Research Paper

A novel thermal management system for cylindrical lithium-ion batteries using internal-external fin-enhanced phase change material

P. Zare [a], N. Perera [a],[*], J. Lahr [a], R. Hasan [b]

[a] *School of Engineering and the Built Environment, Birmingham City University, Birmingham B4 7XG, UK*
[b] *Department of Mechanical Engineering, Military Institute of Science and Technology, Dhaka 1216, Bangladesh*

ARTICLE INFO

ABSTRACT

This study introduced a phase change material (PCM)-based battery thermal management system (BTMS) using an innovative combination of internal and external fins to create PCM silos around the battery surface, addressing the low thermal conductivity of PCM. The lumped-capacitance thermal model and enthalpy-porosity approach were employed for the battery heat generation and PCM melting process, respectively. The BTMS was evaluated under transient and constant heat generation of the battery at various discharge rates. The effects of fin quantity on thermal management performance, energy density, heat storage capacity, and PCM melting time were investigated. The developed BTMS showed superior performance compared to the battery system with natural air convection cooling and the PCM cooling system without fins. At the end of the PCM complete melting process, the BTMS with 4 internal-external fins decreased the battery surface temperature by 9.90 and 17.45 K compared to the PCM cooling system without fins at the discharge rates of 3C and 5C, respectively. The BTMS with 4 internal-external fins kept the battery surface temperature under the optimum temperature of 318.15 K even at a high ambient temperature of 308.15 K while providing up to 10.02% higher energy density, 11.11% higher heat storage capacity, 32.79% higher fin efficiency, and only 1.08% lower overall fin effectiveness compared to greater fin quantities. The proposed BTMS provided an almost uniform cooling effect on the battery surface compared to the system without fins, which has been largely overlooked in previous studies on BTMSs. Various heat transfer regimes were identified during the PCM melting process. Correlations for predicting the PCM liquid fraction and Nusselt number were proposed as a function of a group of dimensionless numbers. These findings provided valuable insights for designing efficient PCM-based BTMSs.

1. Introduction

Clean modes of transport, such as electric vehicles and hybrid electric vehicles, in contrast to conventional internal combustion engine vehicles, are projected as one of the most sustainable solutions for future transport [1]. Utilising electric vehicles can decrease the emission of ozone-depleting substances by 40% [2]. Consequently, many institutions and researchers are motivated to develop a suitable electrical energy storage technology for these clean vehicles to be further commercialised, providing a long driving range and desirable acceleration capability [1].

Lithium-ion batteries are the most common form of rechargeable electrical energy storage technology on the market [3]. These batteries are suitable for a wide range of applications such as portable electronics, electric vehicles, and energy storage systems because of their relatively

high energy density of about 0.4–2.4 MJ·L^{-1}, good cycling performance, low self-discharge, no memory effect, high operating voltage, fast charging capability, and reasonable cost [4,5]. The 3 most common shapes of lithium-ion batteries on the market are pouch, prismatic, and cylindrical. Cylindrical lithium-ion batteries can withstand internal pressures without deformation, have a long calendar life, are increasingly employed in electric vehicles, are economical to manufacture, and have good cycling ability [6]. Therefore, a commercial cylindrical lithium-ion battery was studied in this paper.

Lithium-ion batteries are sensitive to pressure, vibration, and temperature. Among these potential risks, storage and operating temperature affect the battery performance, safety, electrochemical system, charge acceptance, power output, discharge capacity, and cycling life. The temperature rise in lithium-ion batteries may lead to capacity fade, self-discharge, thermal runaway, fire, or even explosion [5,7]. These issues associated with the temperature rise in lithium-ion batteries

Nomenclature

A_{mush}	mushy zone constant
A_w	total heat transfer area (m^2)
C_p	specific heat capacity (J·kg^{-1}·K^{-1})
C_0	battery nominal capacity (Ah)
E_d	energy density (Wh·kg^{-1})
$Fo = \frac{\alpha t}{H^2}$	Fourier number
$\vec{g}$	gravitational acceleration (m·s^{-2})
H	BTMS height (m)
H_{PCM}	PCM enthalpy (J·kg^{-1})
h	convective heat transfer coefficient (W·m^{-2}·K^{-1})
h_{PCM}	PCM sensible enthalpy (J·kg^{-1})
HAR	heat transfer area ratio
I	electric current (A)
k	Thermal conductivity (W·m^{-1}·K^{-1})
L_{PCM}	PCM latent heat (J·kg^{-1})
l_f	fin length (m)
m	BTMS mass (kg)
N	number of fins
n	normal direction
$\overline{Nu}$	surface-averaged Nusselt number
p	pressure (Pa)
Q	generated or absorbed heat (W)
q_b	volumetric heat generation rate (W·m^{-3})
R_e	total internal resistance (Ω)
Ra	Rayleigh number
$Ste^* = \frac{C_{p,s}(T_m-T_a)+C_{p,l}(T_w-T_m)}{L_{PCM}}$	modified Stefan number
T	temperature (K)
t	time (s)
t_{PCM}	PCM thickness (m)
U	battery nominal voltage (V)
$\vec{u}$	velocity vector (m·s^{-1})

$\vec{u}_p$	pull velocity (m·s^{-1})
V	terminal voltage (V)
V_b	battery volume (m^3)
dE/dT	entropy coefficient (V·K^{-1})
ΔH_{PCM}	PCM enthalpy change (J·kg^{-1})

Greek letters

α	thermal diffusivity (m^2·s^{-1})
β	thermal expansion coefficient (K^{-1})
γ	liquid fraction
δ_f	fin thickness (m)
δ_h	housing thickness (m)
δ_i	insulation layer thickness (m)
ε	a constant
μ	dynamic viscosity (kg·m^{-1}·s^{-1})
ρ	density (kg·m^{-3})
τ	dimensionless time

Subscripts

a	reference value or ambient
irr	irreversible reaction
l	liquid
m	melting
rev	reversible reaction
s	solid
t	total reaction
w	surface-averaged on the fins and housing

Acronyms

BTMS	Battery Thermal Management System
PCM	Phase Change Material
HPPC	Hybrid Pulse Power Characterization
NCM	LiNi$_x$Co$_y$Mn$_z$O$_2$

underline the importance of developing an efficient and reliable battery thermal management system (BTMS) to keep the battery temperature in the safe range of 298.15–323.15 K (25–50 °C) [8,9]. And more precisely, the battery temperature should be maintained below 318.15 K (45 °C) for lifespan and under 323.15 K (50 °C) for safety [10,11]. The uneven temperature distribution in a single battery cell can cause thermal stress, leading to irreparable damage to the battery performance, such as capacity loss, increased impedance, and self-discharge. Therefore, controlling temperature differences in a single battery cell is also critical [12].

These thermal management systems are categorised as active, passive, and hybrid BTMSs [13]. While active BTMSs can effectively control the battery temperature [14], developing passive thermal management systems has become popular among researchers due to their simple structures and no need for external energy sources in these systems [15]. PCM is widely studied as a novel passive thermal management system because of its simple structure, low cost, excellent cooling performance, and high latent heat, which enables it to absorb a substantial amount of heat during the phase change process, maintaining the battery temperature around the phase change temperature for some time [16,17]. PCMs can be classified as solid–solid, solid–liquid, solid–gas, and liquid–gas PCMs. Solid-liquid PCMs are the most commonly used type due to their high latent heat capacity and small volume change during the phase change [18]. Solid-liquid PCMs are classified into 3 main categories of organic (paraffin and non-paraffin), inorganic (salt hydrates and metallics), and eutectic mixtures (organic-organic, inorganic-inorganic, and inorganic–organic mixtures). Organic PCMs have higher latent heat, less separation, and less undercooling than inorganic

PCMs [19,20]. Zare, et al. [15] investigated the advantages and disadvantages of solid–liquid organic PCMs in detail, which are the most common type of PCMs in the BTMSs, along with several recently used techniques to deal with their possible challenges in thermal management systems. Paraffin wax, which is a solid–liquid organic PCM, was used in this study to propose an effective BTMS.

One of the significant technical challenges associated with PCMs is their low thermal conductivity, which impedes the heat transfer rate within the PCMs and lowers their cooling capacity. When the PCM is completely melted, the heat absorbed by the PCM has to be dissipated to the surroundings in time, highlighting the importance of improving the PCM thermal conductivity [21]. Various techniques have been proposed to overcome the issues related to the poor thermal conductivity of PCMs. Fillers with high thermal conductivity, such as carbon fibre, graphene, and carbon nanotubes, have been suspended into the PCM to enhance the PCM thermal conductivity. However, these fillers might not form a homogeneous composite. Although embedding the PCM in highly conductive structures such as porous materials and foams can be another heat transfer enhancement technique, the PCM might become inhomogeneous after multiple thermal cycles [2]. In PCM-based BTMSs, studies on extending the heat transfer area to enhance the heat transfer rate are quite limited compared to increasing the PCM thermal conductivity [22]. Inserting metal fins within the PCM can be an efficient heat transfer enhancement technique due to their simple structure and ease of manufacturing; hence it is widely used for the cooling of electronics and in thermal energy storage systems [21]. Therefore, more in-depth investigations of fin-enhanced PCM-based systems for the thermal management of lithium-ion batteries can provide useful guidelines for

practical applications.

Various factors such as fin shape, fin size, fin quantity, and fin material must be considered when designing fins to enhance the heat transfer rate within PCM [23]. Weng, et al. [24] compared the thermal performance of rectangular fins and three branch fins shaped in X, Y, and V. The branch fins showed excellent performance in decreasing the battery temperature compared to the rectangular fins due to the increased heat transfer area. The BTMS with X-shaped fins delivered the best thermal management capability and maintained the maximum temperature of the battery below 320 K at a high ambient temperature of 313 K. Fins arranged along the axial or radial direction of the battery are named longitudinal or radial fins, respectively. Weng, et al. [25] concluded that longitudinal fins dissipate the accumulated heat at the bottom of the BTMS, while radial fins facilitate heat conduction due to the larger surface area. Therefore, they proposed a combination of 4 longitudinal and 2 radial fins to achieve minimum space utilisation and maximum cooling efficiency. Khaboshan, et al. [26] investigated the thermal performance and thermal energy storage capabilities of BTMSs with various combinations of PCM, metal foam, and fins under a 3C discharge rate. The optimum BTMS, which was the combination of PCM, metal foam, and fins, reduced the battery surface temperature by 3 K compared to the pure PCM cooling. Furthermore, the fins in the optimum BTMS acted as a network of heat sources to spread heat in the system, and the metal foam uniformly distributed the generated heat between the battery and the environment. Sun, et al. [27] designed a fin structure comprising of straight and arc fins for cylindrical batteries, which prolonged the working time of the battery by 54–90% compared to the PCM cooling system without fins due to the increased heat transfer area.

Researchers employed fins within the PCM (internal fins) to enhance the conduction heat transfer [23,28] or on the outer surface of the PCM (external fins) to improve its surface heat transfer capability [29,30]. As shown in Fig. 1, the present study proposed a combination of internal and external fins in the PCM-based BTMS. These novel metal fins comprised a cylindrical and 4 longitudinal internal-external fins within a metal housing. These fins and housing created PCM silos around the cylindrical lithium-ion battery to take advantage of conduction and natural convection heat transfer within the PCM and natural convection heat transfer to the surrounding environment. The aim was to provide a uniform cooling effect around the circular perimeter and along the height of the battery, which has been largely overlooked in previous studies on BTMSs [31–33]. The dashed lines in Fig. 1 (c) show the symmetry planes with α and β being 45° and 90°, respectively. In the present study, all the simulations were carried out for a single lithium-ion battery to assess the thermal effects of the proposed fin design without the complexities introduced by interactions between multiple batteries in a battery module, simplify the interpretation of the results, and establish a baseline thermal performance that can serve as a reference for future studies involving multiple batteries or more complex systems.

2. Problem statement

This study used a commercial 18,650 lithium-ion battery (LiNi$_x$-Co$_y$Mn$_z$O$_2$ or NCM) due to the higher energy density of NCM batteries than other battery types employed in electric vehicles manufactured by Tesla, Nissan Leaf, Chevy Volt, and BMW [34–36]. The specification of the selected NCM battery is provided in Table 1. Since the detailed structure of a cylindrical battery has little impact on its thermal performance in the lumped model, which will be elaborated in section 3.1, the battery was considered a homogeneous cylinder to simplify the simulation model while maintaining the accuracy of the results [7]. The axial and radial thermal conductivities of the cylindrical lithium-ion battery differ due to the differences in material compositions in various directions. These can be considered as the series and parallel connections of each layer, respectively, by neglecting the internal contact resistance [37].

The physical model of the proposed BTMS is depicted in Fig. 1(a). As shown in Fig. 1(a) and (b), the developed BTMS comprised a housing, cylindrical and internal-external fins, PCM, battery, and an insulation layer. The selection of the BTMS's dimensions was based on common practice within the scientific community [27,38–40]. The battery, with a diameter of 18 mm, was located in the centre of the cylindrical housing. The battery was surrounded by a cylindrical and 4 longitudinal internal-external metal fins with a length (l_f) of 11 mm. The height of the fins and the battery, H, which was the same, was 65 mm. The thicknesses of fins, δ_f, the housing, δ_h, and the insulation layer, δ_i, were fixed as 1 mm. The regions between the fins and the housing were filled with paraffin wax, which had a thickness, t_{PCM}, of 5 mm.

Fin materials must have high thermal conductivity to decrease

Table 1
Specification of the selected lithium-ion battery [7].

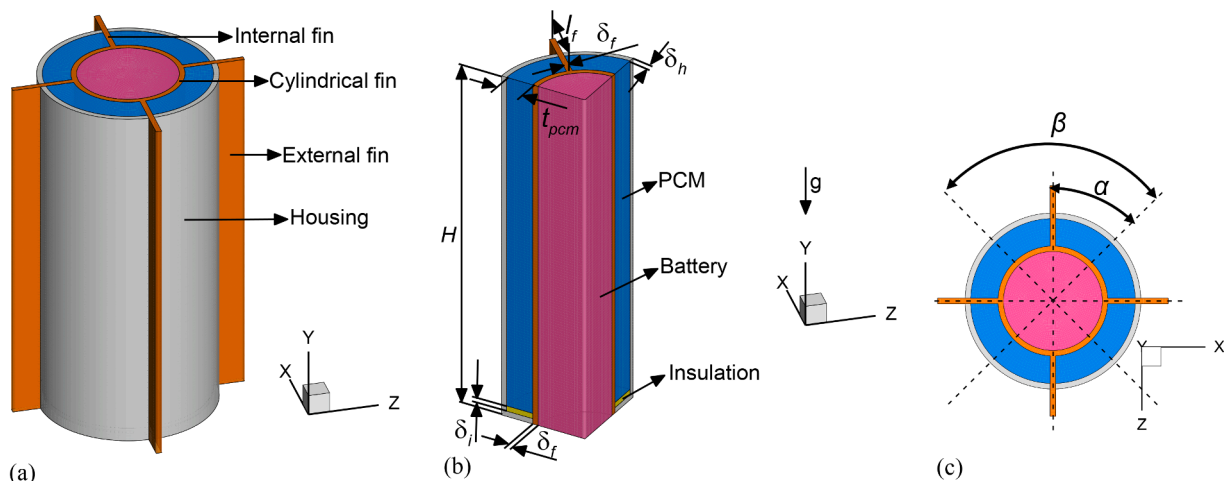| Parameter	Value	Parameter	Value
Nominal voltage (V)	3.7	Thermal conductivity in the radial direction (W·m^{-1}·K^{-1})	0.2
Nominal capacity (Ah)	2.6	Thermal conductivity in the axial direction (W·m^{-1}·K^{-1})	37.6
Cell mass (kg)	0.0475	Specific heat capacity (J·kg^{-1}·K^{-1})	1200

Fig. 1. The diagram of the proposed BTMS (a) the isometric view, (b) its dimensions, and (c) the top view.

conduction thermal resistance, high specific heat capacity to ensure high thermal storage per unit of volume, and low density to provide high thermal storage per unit of mass. In light of this, copper and aluminium are the materials widely used for the fins [22]. In this study, a type of aluminium alloy was selected for the BTMS housing and the fins because of its lighter weight, higher thermal conductivity, and higher specific heat compared to these two commonly used materials. Aluminium alloy has good anti-corrosive properties, availability, and reasonable cost [6]. The thermo-physical properties of paraffin wax, aluminium alloy, and insulation material are listed in Table 2.

3. Numerical methodology and governing equations

3.1. Heat generation in lithium-ion batteries

Lumped-capacitance thermal model and electrochemical reaction model are the two commonly used techniques to describe heat generation in lithium-ion batteries. The key advantage of the lumped-capacitance thermal model over the electrochemical model is its low computational cost [42]. To verify the applicability of the lumped-capacitance thermal model, it is necessary to calculate the Biot number ($\mathrm{Bi} = \frac{hL_c}{k_{battery}}$), where h is the convective heat transfer coefficient, L_c is the characteristic length calculated as the ratio of the volume to the surface area of the cylindrical battery, and $k_{battery}$ is the thermal conductivity of the battery. For low Biot numbers, mostly lower than 0.1, the lumped-capacitance thermal model can be applied [43,44].

In this study, the lumped-capacitance model used for the actual transient heat generation of the lithium-ion battery considers resistive and entropic heat generation, which was neglected in some published literature on BTMSs [28,40]. In the lumped-capacitance model, the battery is considered to have constant thermo-physical properties throughout the battery, and the heat generation is a function of the voltage and current characteristics [42]. When the operating conditions remain constant, the total heat generation during the discharging process is higher than that during the charging process due to the difference in the reaction heat generation between the charging and discharging processes [45]. Therefore, only the discharging process was explored in this study to cover a wide range of battery operation conditions. The heat generation of lithium-ion batteries is mathematically expressed as the Bernardi equation [7]:

$$Q_t = Q_{irr} + Q_{rev} \tag{1}$$

$$Q_{irr} = I(E - V) = I^2 R_e \tag{2}$$

$$Q_{rev} = -T\Delta S\left(\frac{I}{nF}\right) = -I\left[T\left(\frac{dE}{dT}\right)\right] \tag{3}$$

where the total heat generation in the battery (Q_t), irreversible heat (Q_{irr}), reversible heat (Q_{rev}), open circuit voltage (E), terminal voltage (V), electric current (I), temperature (T), total internal resistance (R_e), change in entropy (ΔS), number of the flow of electrons (n), Faraday's constant (F), and entropy coefficient ($\frac{dE}{dT}$) are identified. Therefore, to find the battery heat generation, R_e and $\frac{dE}{dT}$ should be determined. Jia-qiang, et al. [7] conducted the Hybrid Pulse Power Characterization (HPPC) test to develop the function of the total internal resistance (R_e) and performed the experiments to develop the function of the entropy coefficient ($\frac{dE}{dT}$). Hence, the heat generation rate per unit of the battery volume (V_b) can be calculated by:

$$q_b = \frac{Q_t}{V_b} \tag{4}$$

In this study, simulations were conducted for transient heat generation of the battery at various discharge rates of 1C, 2C, 3C, and 5C and average constant heat generation conditions at two discharge rates of 3C and 5C, representing fast discharging. The discharge rate (C-rate) is defined as the discharge current divided by the battery's nominal capacity (C_0) [46]. The discharge rates of 1C to 5C are often used in experimental studies [47] to assess the performance of cylindrical NCM lithium-ion batteries under various load demands without damaging the battery. The transient heat generation of the battery was calculated using equations (1)–(4) to examine the actual thermal behaviour of the BTMS under various discharging conditions. The simulations for the transient heat generation of the battery were conducted at a high ambient temperature of 308.15 K to simulate extreme environmental conditions. The constant heat generation of the battery was studied to analyse the thermal performance of the BTMS under a certain heat generation level. Table 3 presents the experimental values for the average constant heat generation of the NCM 18650 lithium-ion battery with a nominal capacity of 2.6 Ah and a nominal voltage of 3.7 V obtained by Huang, et al. [47] at the ambient temperature of 298.15 K, which were used in this study.

3.2. PCM melting process

In recent times, various approaches for the modelling of the solid–liquid phase transition process have been developed. The enthalpy-porosity approach is the most commonly used technique to accurately describe the natural convection in the melt region. It precisely predicts the phase transition position and the shape of the melt front, which needs relatively modest computational requirements. In this approach, the phase change process occurs in a finite melting temperature range, generating an artificial mushy zone where the liquid fraction (the volume fraction of the liquid phase) changes from 0 for the solid phase to 1 for the liquid phase. The velocity of the fluid element in the mushy zone also varies from 0 for the solid phase to the natural convection velocity for the liquid phase. This technique simulates this velocity transition by simulating flow in the mushy region as flow through a porous medium. Therefore, a sink term, $\overrightarrow{S}$, in the form of the Carman-Koseny equation, which is derived from the Darcy law for fluid flow in porous media, is added to the Navier-Stokes equations to simulate the impact of damping in the mushy region and the pressure drop due to the solid phase existence, which is expressed as [48]:

$$\overrightarrow{S} = -A(\gamma) \bullet \left(\overrightarrow{u} - \overrightarrow{u}_p\right) \tag{5}$$

Table 2
The thermo-physical properties of the materials [27,41].

Materials	Properties	Value
Paraffin wax	Thermal conductivity (W·m^{-1}·K^{-1}), solid	0.20
	Thermal conductivity (W·m^{-1}·K^{-1}), liquid	0.18
	Specific heat capacity (J·kg^{-1}·K^{-1}), solid	2000
	Specific heat capacity (J·kg^{-1}·K^{-1}), liquid	2350
	Density (kg·m^{-3}), solid	880
	Density (kg·m^{-3}), liquid	700
	Melting temperature (K)	313.75–317.85
	Latent heat (J·kg^{-1})	240,800
	Dynamic viscosity, (kg·m^{-1}·s^{-1})	0.005
	Thermal expansion coefficient (K^{-1})	0.00076
Al alloy	Thermal conductivity (W·m^{-1}·K^{-1})	167
	Specific heat capacity (J·kg^{-1}·K^{-1})	896
	Density (kg·m^{-3})	2700
Insulation	Thermal conductivity (W·m^{-1}·K^{-1})	0.19
	Specific heat capacity (J·kg^{-1}·K^{-1})	1260
	Density (kg·m^{-3})	1200

Table 3
The constant heat generation of the NCM 18650 lithium-ion battery [47].

Discharge rate	Q_t(W)	q_b(W·m^{-3})
3C	2.9158	185,435
5C	6.4809	412,200

where $\vec{u}$ is the velocity vector and $\vec{u}_p$ is the pull velocity. The pull velocity is the solid velocity caused by pulling the solid material out of the domain, which is 0 in this study. The porosity function, $A(\gamma)$, which was proposed by Brent, et al. [49], is expressed as:

$$A(\gamma) = \frac{A_{mush}(1-\gamma)^2}{\gamma^3 + \varepsilon} \tag{6}$$

where ε is a small computational constant used to prevent zero in the denominator, and its value is 0.001 in this work. The mushy zone constant, A_{mush}, reflects the morphology of the melting front and indicates how quickly the fluid velocity approaches 0 as it solidifies, and the suggested value for the mushy zone constant by different researchers ranges from 10^3 to 10^8 for various PCMs, enclosure geometries, and boundary conditions [48,50]. In equations (5) and (6), γ denotes the liquid fraction, which is defined as:

$$\gamma = \begin{cases} 0 & T < T_s \\ \dfrac{T - T_s}{T_l - T_s} & T_s < T < T_l \\ 1 & T > T_l \end{cases} \tag{7}$$

where T_s and T_l represent the solidus and liquidus temperatures during the PCM phase transition, respectively.

3.3. Governing equations

The governing continuity and momentum equations are expressed as [21]:

$$\nabla \bullet (\rho \vec{u}) = 0 \tag{8}$$

$$\frac{\partial(\rho \vec{u})}{\partial t} + \nabla \bullet (\rho \vec{u}\vec{u}) = -\nabla p + \nabla \bullet \tau + \rho_a[1 - \beta(T - T_a)]\vec{g} + \vec{S} \tag{9}$$

where ρ is the density, p is the pressure, τ is the stress tensor, ρ_a is the reference density at the reference temperature of T_a, β is the thermal expansion coefficient, and $\vec{g}$ is the gravitational acceleration, which is set to -9.81 m·s^{-2} in the Y-direction to predict the natural convection in the melted PCM. The present numerical simulations included the natural convection effect during the PCM melting process using the Boussinesq approximation. This approximation is for the linear density-temperature relation associated with the buoyancy forces due to the small density variation, which also provides faster convergence than other temperature-dependent models [27,51]. Energy equations [21] for the battery, fins, PCM, and housing are as shown below, respectively:

$$\rho_{battery}C_{p,battery}\frac{\partial T_{battery}}{\partial t} = \nabla(k_{battery}\nabla T_{battery}) + q_b \tag{10}$$

$$\rho_{fin}C_{p,fin}\frac{\partial T_{fin}}{\partial t} = \nabla(k_{fin}\nabla T_{fin}) \tag{11}$$

$$\frac{\partial(\rho_{PCM}H_{PCM})}{\partial t} + \nabla \bullet (\rho_{PCM}\vec{u}H_{PCM}) = \nabla(k_{PCM}\nabla T_{PCM}) \tag{12}$$

$$\rho_{housing}C_{p,housing}\frac{\partial T_{housing}}{\partial t} = \nabla(k_{housing}\nabla T_{housing}) \tag{13}$$

where H_{PCM} is calculated as:

$$H_{PCM} = \underbrace{h_{PCM}}_{Sensible\,enthalpy} + \underbrace{\Delta H_{PCM}}_{Latent\,enthalpy} \tag{14}$$

$$h_{PCM} = h_a + \int_{T_a}^{T} C_{p,PCM}dT \tag{15}$$

$$\Delta H_{PCM} = \gamma L_{PCM} \tag{16}$$

where h_a is the reference enthalpy at the temperature taken as the reference (T_a), C_p is the specific heat capacity at constant pressure, and L_{PCM} is the specific enthalpy of melting or the latent heat of PCM.

The governing equations were solved in the light of the appropriate initial and boundary conditions by using the commercial computational fluid dynamics (CFD) package ANSYS FLUENT 22/R1, which is based on the finite volume method (FVM) as detailed by Patankar [52]. User Defined Functions (UDFs) for the transient heat generation of the battery were developed by employing equations (1)–(4), which were interpreted into the ANSYS Fluent as the heat source term of the battery domain. The transient PISO algorithm was utilised for pressure–velocity coupling. The PRESTO and second-order upwind schemes were also used to discretise the pressure correction equation and other equations, respectively. The convergence criteria of the residuals of the computational variables were 10^{-4} for continuity and momentum equations and 10^{-10} for the energy equation.

3.4. Initial conditions, boundary conditions, and assumptions

The initial condition of the BTMS was set to:

$$T(x, y, z) = T_a; t = 0 \tag{17}$$

where T_a is the ambient temperature. The adiabatic boundary condition was set at the top and bottom surfaces of the BTMS. No slip boundary conditions were also adopted to assign the velocity of liquid PCM at the fins and housing walls to zero. The thermal contact resistances of all interfaces were ignored. The natural convection boundary condition on the fins and housing wall was:

$$-k_{wall}\frac{\partial T_{wall}}{\partial n} = h(T_{wall} - T_a) \tag{18}$$

where h represents the convective heat transfer coefficient. The convective heat transfer coefficient of air under natural conditions usually ranges from 5 W·m^{-2}·K^{-1} to 10 W·m^{-2}·K^{-1} [47]. In this study, the convective heat transfer coefficient of air was fixed at 10 W·m^{-2}·K^{-1} for the outer wall surface of the housing and the external parts of the fins, which has also been employed in many previous studies on PCM-based BTMS with natural air convection [27,53]. This is a high value of the natural convective heat transfer coefficient under harsh environments that implies a higher ambient air velocity [54]. The effect of various convective heat transfer coefficients, ranging from 5 W·m^{-2}·K^{-1} to 10 W·m^{-2}·K^{-1}, will also be investigated in future work.

The following assumptions were made to simplify the present numerical simulations: (a) the solid and liquid phases of PCM were homogenous and isotropic; (b) the change in the PCM volume due to the phase transition was ignored; (c) the radiation heat transfer was neglected; (d) the flow of the melted PCM was assumed to be laminar and incompressible with negligible viscous dissipation; and (e) the liquid PCM was Newtonian fluid.

4. Numerical model validation

4.1. Heat generation in lithium-ion batteries

The numerical model for the transient heat generation of the selected lithium-ion battery was validated against the numerical and experimental results in [7] for 0.5C and 1C discharge rates with boundaries of the battery subjected to the air natural convection. The Biot number was calculated to be approximately 0.1 and 0.001 in radial and axial directions, respectively, which was small enough to employ the lumped-capacitance thermal model for the heat generation of the battery. Fig. 2 compares the temperature of the middle height of the battery surface obtained by Jiaqiang et al. [7] to that in the present study. The current results, with a maximum error of about 0.5%, were accurate enough to reproduce the experimentally measured and numerical results
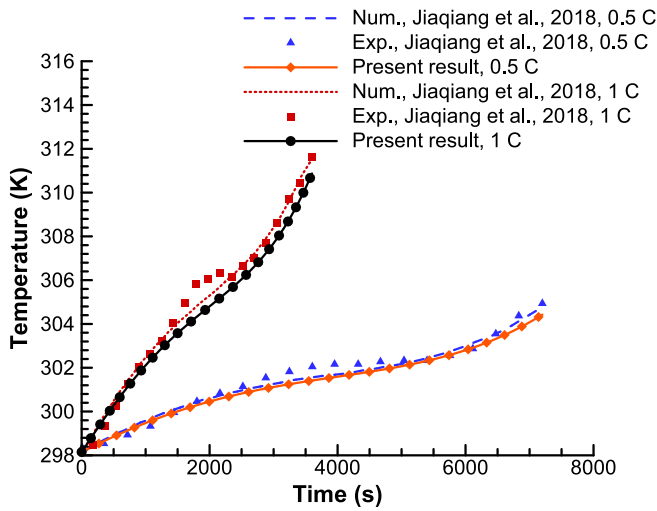
Fig. 2. Validation of the present numerical results with the numerical and experimental results by Jiaqiang, et al. [7] for the thermal behaviour of the selected battery.

of the thermal behaviour of the battery without any cooling system obtained by Jiaqiang et al. [7].

4.2. PCM melting process

Although the Carman-Koseny equation is employed in a majority of available models, it is essential to select an appropriate A_{mush} to accurately predict the heat transfer characteristics within the PCM [48,50]. Since the effect of A_{mush} on both paraffin wax melting process and the average temperature of the battery in the BTMS proposed by Sun, et al. [27] was not carried out, a sensitivity study of A_{mush} was conducted, as shown in Fig. 3. At the start and end of the PCM melting process, the effect of A_{mush} on the PCM liquid fraction and average temperature was insignificant when heat was primarily transferred through conduction. Fadl and Eames [48] also showed that the effect of A_{mush} is less noticeable in regions with dominant conductive heat transfer and is more prominent where natural convection heat transfer dominates. Table 4 shows the maximum deviation of the results for various A_{mush} values compared to the results for $A_{mush} = 10^8$. Increasing A_{mush} value from 10^7 to 10^8 resulted in a maximum error of 0.01 and 0.33% for the liquid fraction and temperature, respectively. The higher values of A_{mush}, more than 10^8, were also tested, which lead to the oscillation of the solution and resulted in divergence. This divergence and oscillating behaviour of the solution were also reported in more detail by Brent, et al. [49]. Therefore, A_{mush} was assumed to be 10^7 in the present study.

Sun, et al. [27] experimentally and numerically examined the

thermal management performance of a PCM-fin system with straight and arc fins inserted into the PCM. A heater with a heat generation of 16 W was used to replicate the discharging process of the battery, increasing the battery temperature from the initial temperature of 293.15 K (20 °C) to the safety limit of 333.15 K (60 °C). Subsequently, the heater was deactivated to simulate the rest time of the battery, decreasing the battery temperature from 333.15 K to 313.15 K (40 °C). Fig. 4 compares the present numerical results with the numerical and experimental results obtained by Sun, et al. [27] for the change in PCM liquid fraction during the battery heat generation until the PCM was completely melted and the average temperature of the battery during the melting and solidification cycling test. The PCM liquid fraction and temperature variation curves show similar trends to those of the previously published work [27] with a maximum deviation of 0.04 and 3.96%, respectively, as shown in Table 5. These results further confirmed the reliability of the present numerical model. The discrepancy between the numerical studies and experimental work can be due to simplifying the model used in the simulations. For instance, the PCM thermo-physical properties were assumed to be constant in the simulations, while these properties might change during the experiments. In addition, the time lapse at the end of the melting process and the start of the solidification process in Fig. 4 (b) can be ascribed to the constant value of the convective heat transfer coefficient between the BTMS and the surroundings in the simulations. This coefficient might be higher during the experiments due to the variations in the ambient temperature or air flow patterns, resulting in faster heat dissipation from the BTMS to the surroundings and slower temperature rise during the experiments.

4.3. Grid and time step independence tests

The numerical solutions critically depend on the mesh and time step size. To eliminate the effect of these two parameters on the results, mesh and time step independence tests were carried out. A reference case of the BTMS with 4 internal-external fins at the highest discharge rate of 5C was selected for the independence studies. Five mesh sizes of 1.5, 1, 0.8, 0.5, and 0.4 mm were selected, which included 28,035, 91,344, 151,146, 573,820, and 1,203,235 elements, respectively. The results of the grid independence test are shown in Fig. 5 (a) for the maximum temperature on the battery surface. Table 6 shows more details on the grid information, including grid size, number of elements, average element quality, and maximum discrepancy in the maximum temperature on the battery surface compared to the most refined mesh, which is the grid size of 0.4 mm. The grid size of 0.5 mm with an average element quality of 0.90 was sufficient for this work, which showed a maximum percentage error of 0.01%. Fig. 5 (c) shows the mesh generated in the PCM-based BTMS with a cylindrical and 4 longitudinal internal-external fins.

The effect of the time step sizes of 0.1, 0.25, 0.5, and 1 s on the results was investigated to make the solution independent of the time step size,
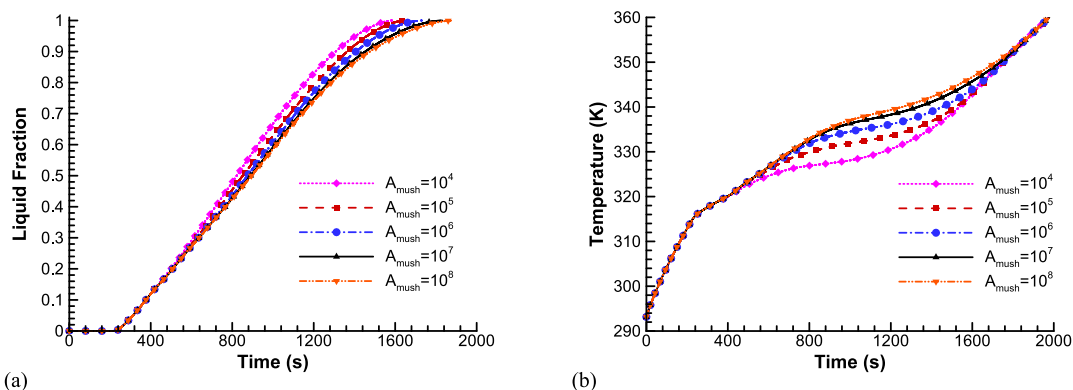

Fig. 3. The effect of A_{mush} on (a) PCM liquid fraction and (b) the average temperature of the battery.

Table 4

The maximum deviation of the results for various A_{mush} values compared to the results for..$A_{mush} = 10^8$

A_{mush}	Liquid Fraction				Temperature (K)			
	Time (s)	Value	Value for $A_{mush} = 10^8$	Absolute error	Time (s)	Value	Value for $A_{mush} = 10^8$	Percentage error
10^4	1211.5	0.84	0.75	0.09	1074.5	328.82	337.98	2.71%
10^5	1462.5	0.95	0.89	0.06	1191	333.51	339.24	1.69%
10^6	1525.75	0.95	0.92	0.03	1316.75	337.57	340.87	0.97%
10^7	1579.75	0.95	0.94	0.01	1340	340.11	341.23	0.33%
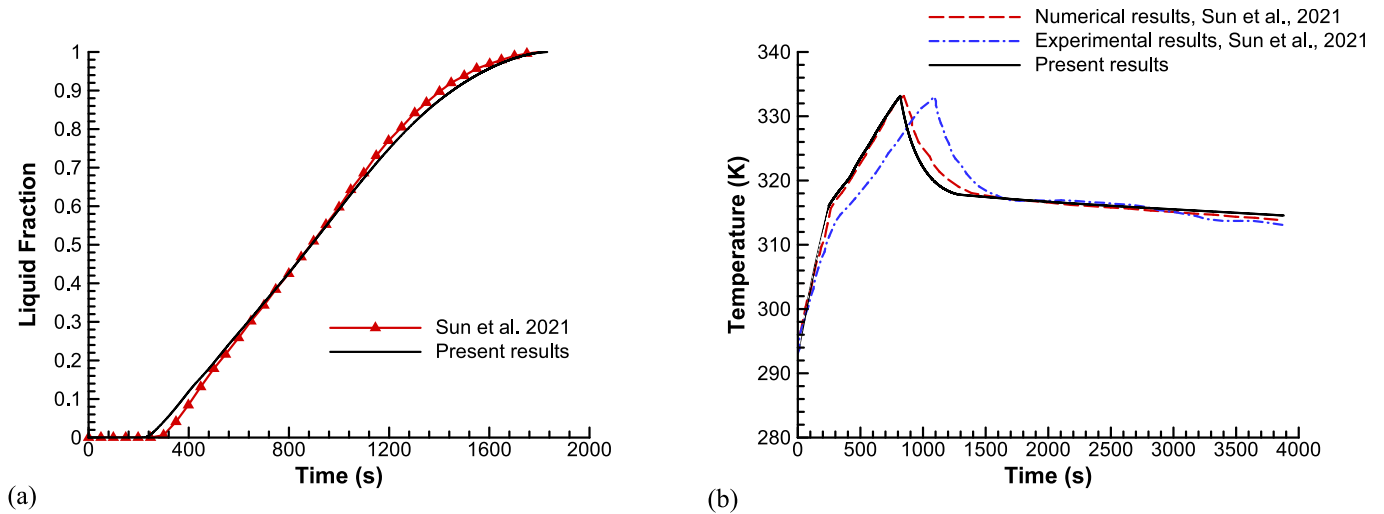
Fig. 4. Comparison of the present numerical results with the numerical and experimental results by Sun, et al. [27] for (a) PCM liquid fraction and (b) average temperature of the battery during the melting and solidification cycling test.

Table 5

The maximum deviation of the present numerical results from the numerical and experimental results by Sun, et al. [27].

Time (s)	Liquid Fraction			Temperature (K)			
	Present results	Numerical results [27]	Absolute error	Present results	Numerical results [27]	Experimental results [27]	Percentage error
349	0.08	0.04	0.04	–	–	–	–
912	–	–	–	325.73	329.65	–	1.19%
1090	–	–	–	319.88	–	333.07	3.96%

as shown in Fig. 5 (b). Table 6 also shows more details on the time step independence test for the maximum temperature on the battery surface compared to the time step size of 0.1 s. The maximum deviation of the results for the maximum temperature on the battery surface for the time step sizes of 1 s and 0.5 s was negligible. Therefore, the time step size of 0.5 s was applied for all the simulations in this work to reduce the computing requirements while maintaining accuracy.

4.4. Symmetry model validation

As presented in Fig. 1 (c), the BTMS model with 4 internal-external fins was simplified to 1/8 and 1/4 models due to the symmetric geometry and physics of the BTMS by employing the symmetry boundary conditions. Fig. 6 shows negligible variation in volume average of the PCM liquid fraction and maximum temperature on the battery surface for the two simplified models compared to the whole BTMS model with a maximum error of 0.002 and 0.009%, respectively, which verified the reliability and reasonable accuracy of the simplified models. Therefore, the 1/8 model was used in the subsequent investigations, which helped to save computational costs and time.

5. Results and discussion

5.1. Effects of the discharge rate

The effectiveness of the proposed BTMS with 4 internal-external fins was investigated under transient heat generation of the lithium-ion battery at various discharge rates of 1C, 2C, 3C, and 5C. The maximum temperature on the battery surface for the fully charged battery until the end of the discharge process was considered for the evaluation, as shown in Fig. 7 (b). The PCM liquid fraction plot also shows the usage of PCM in this BTMS, as shown in Fig. 7 (a). The heat storage in the PCM-based BTMS could be divided into three phases of sensible heat storage before the PCM phase change process, latent heat storage during the phase change, and sensible heat storage after the PCM is completely melted. As shown in Fig. 7 (b), at the relatively low discharge rate of 1C, the battery temperature was below the PCM solidus temperature. Therefore, the PCM did not melt, and only sensible heat storage occurred. Almost linear temperature rise was observed at higher discharge rates of 2C, 3C, and 5C during the sensible heat storage within the PCM up to the PCM solidus temperature of 313.75 K. With more heat absorption by the PCM, up to 4.52%, 13.45%, and 26.81% of the PCM latent heat capacity was exploited during the PCM phase change process at 2C, 3C, and 5C discharge rates, respectively (shown in Fig. 7 (a)). This
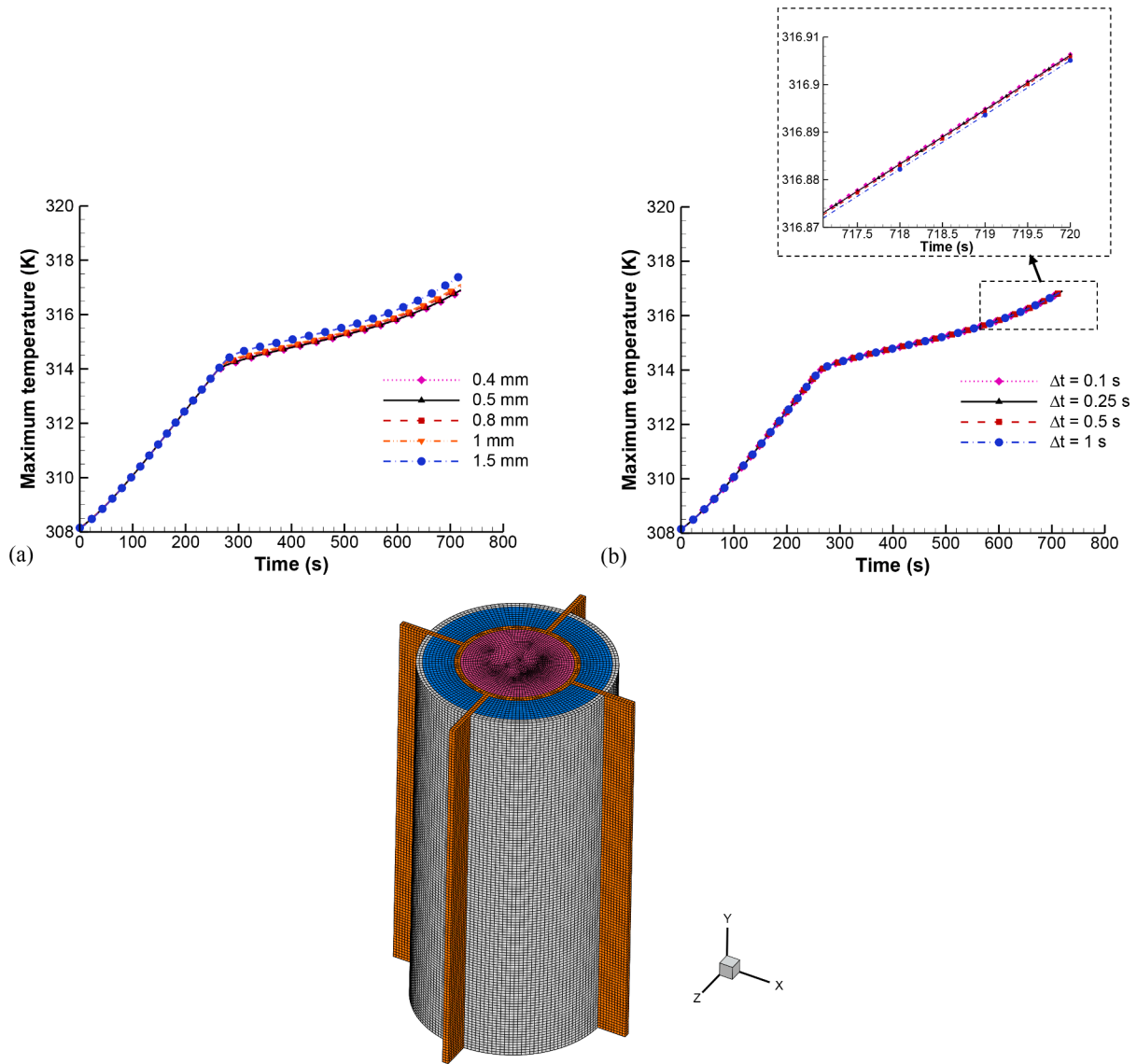
Fig. 5. (a) Grid independence test, (b) time step independence test, and (c) the mesh generated in the BTMS.

Table 6
Information on the grid and time step independence tests in comparison to the smallest mesh and time step sizes.

		Number of elements	Average element quality	Percentage error for temperature
Mesh size	0.4 mm	1,203,235	0.92	0%
	0.5 mm	573,820	0.90	0.01%
	0.8 mm	151,146	0.85	0.05%
	1 mm	91,344	0.81	0.07%
	1.5 mm	28,035	0.80	0.18%
Time step	0.1 s	573,820	0.90	0%
	0.25 s	573,820	0.90	0.00007%
	0.5 s	573,820	0.90	0.0002%
	1 s	573,820	0.90	0.0004%

resulted in a significant decrease in the temperature rise rate, and the maximum temperature on the battery surface was maintained well below the optimum temperature of 318.15 K for the battery's safety and lifespan. The maximum temperature on the battery surface reached 311.91, 314.35, 315.20, and 316.89 K at the end of the discharge rates of 1C, 2C, 3C, and 5C, respectively. Fig. 7 (b) also shows a slight ascent of the maximum temperature at the end of the discharge processes, which could be due to the higher battery internal resistance because of the higher battery temperature, as expressed in the equation for the total internal resistance in [7].

5.2. Effects of the number of internal-external fins

It is worthwhile to obtain an optimum number of internal-external fins in the proposed PCM-based BTMS to enhance its thermal performance. Fig. 8 depicts the PCM-based BTMSs that contain 4, 6, 8, 10, and 12 internal-external fins. The value of α in Fig. 1 (c) for the BTMSs with 4, 6, 8, 10, and 12 was 45°, 30°, 22.5°, 18°, and 15°, respectively.

Fig. 9 illustrates the change in the maximum temperature on the battery surface in the PCM-based BTMSs with different fin quantities and the PCM cooling system without fins but with the same PCM thickness as fin-enhanced PCM-based BTMSs under transient heat generation of the
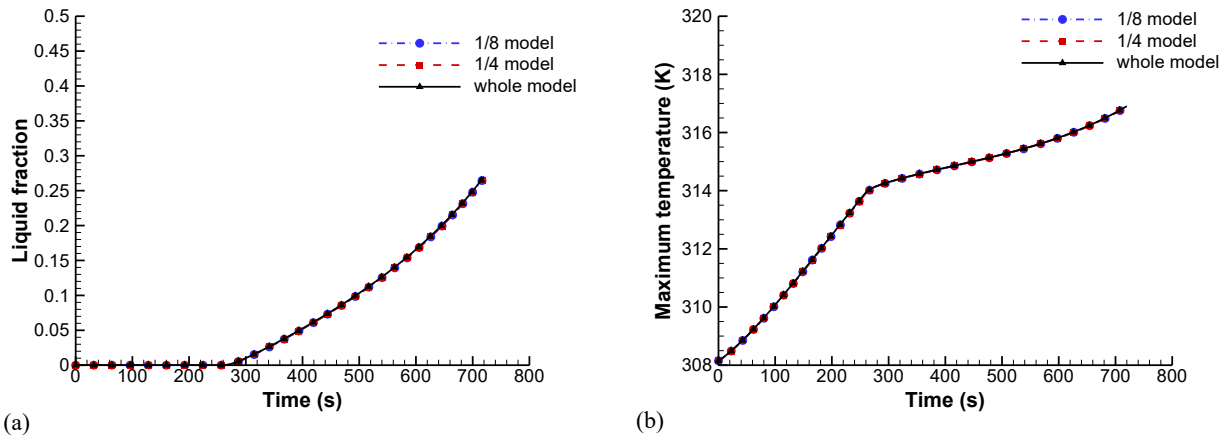
(a)

(b)

Fig. 6. Comparison of the 1/8, 1/4, and whole models of the BTMS with 4 internal-external fins at 5C discharge rate (a) the PCM liquid fraction and (b) the maximum temperature on the battery surface.
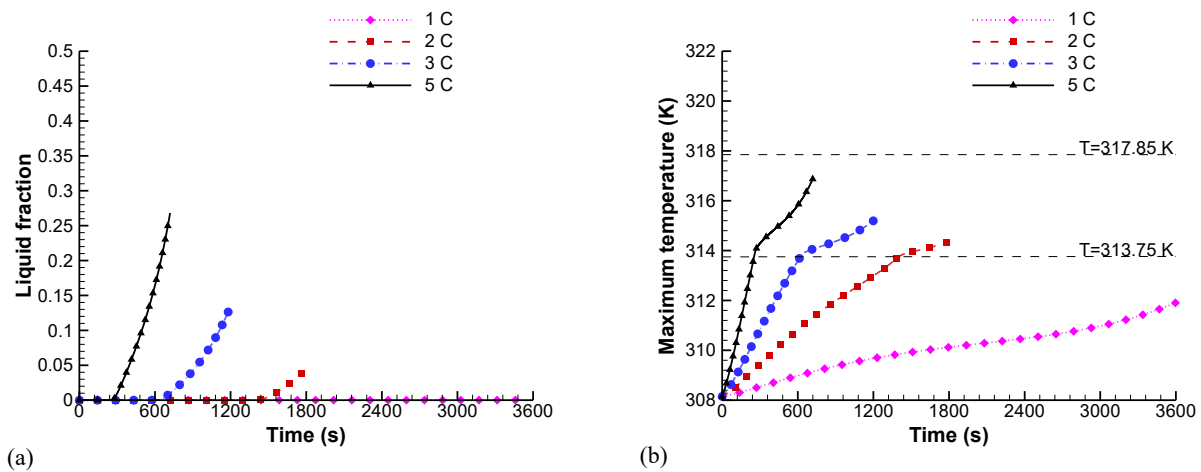

(a)

(b)

Fig. 7. The effect of the discharge rate on (a) the PCM liquid fraction and (b) the maximum temperature on the battery surface.
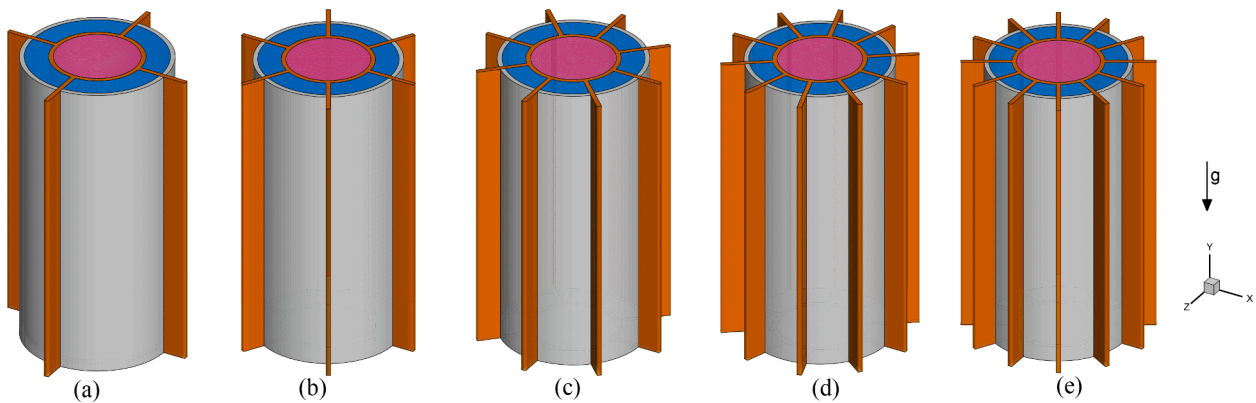

(a) (b) (c) (d) (e)

Fig. 8. The PCM-based BTMSs with (a) 4, (b) 6, (c) 8, (d) 10, and (e) 12 internal-external fins.

battery at various discharge rates of 1C, 2C, 3C, and 5C. All these BTMSs maintained the maximum temperature on the battery surface under the optimum temperature of 318.15 K for the safety and lifespan of the battery, except for the PCM cooling system without fins at high discharge rates of 3C and 5C. An increment in the number of fins enhanced the contact surface area between the fins and PCM, thus enhancing the heat transfer within the PCM, and expedited heat dissipation to the surroundings through natural air convection by increasing

the heat transfer area of external fins. Therefore, the rate of temperature rise was decreased by increasing the number of internal-external fins. Furthermore, this reduction in the maximum temperature by increasing the fin quantity was less significant at higher discharge rates. This might be due to the high heat generation of the battery that even increasing the number of fins from 4 to 12 did not significantly improve heat transfer and heat absorption by the PCM and heat dissipation to the surroundings.
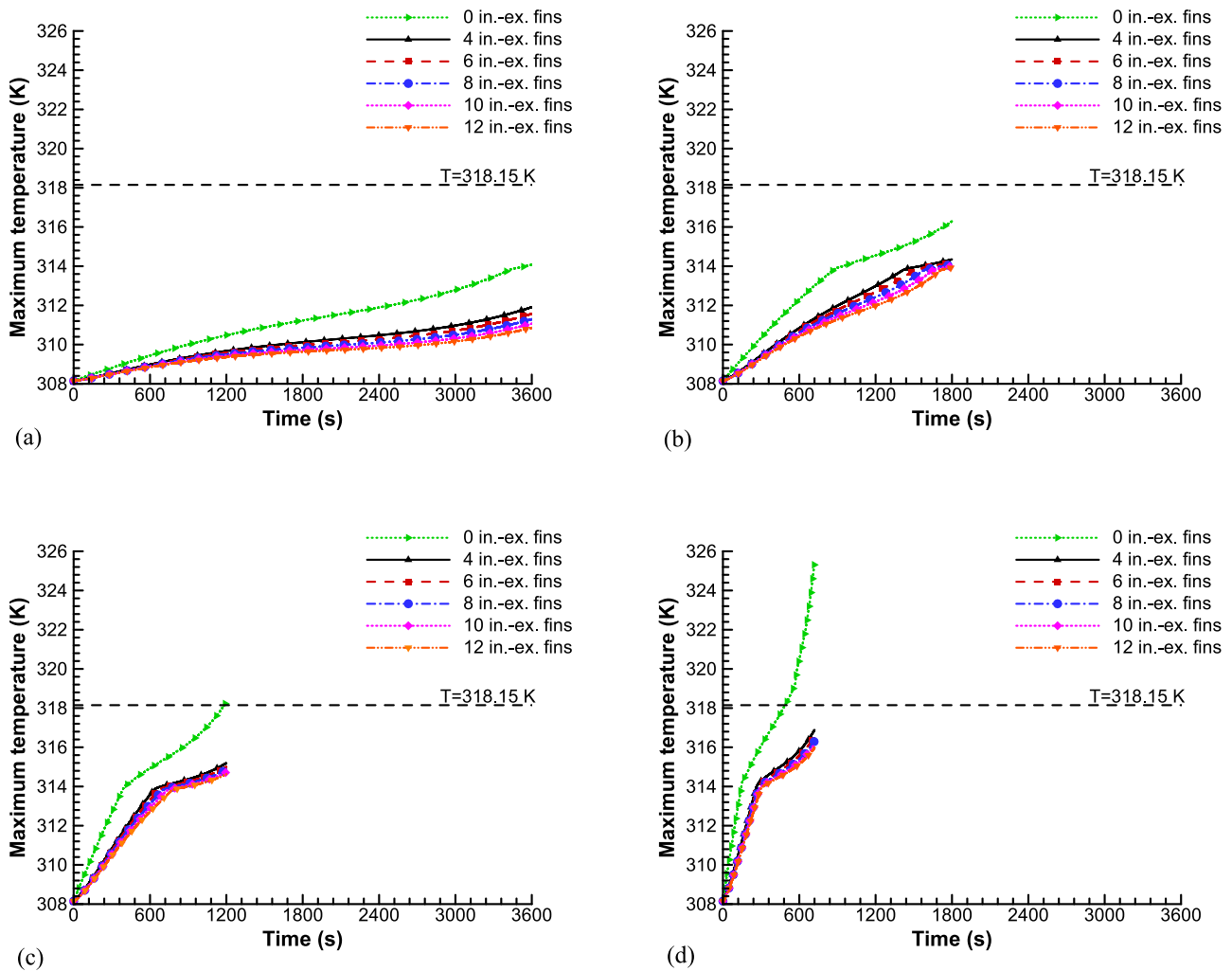
Fig. 9. The maximum temperature on the battery surface in the BTMSs with different quantities of internal-external fins at (a) 1C, (b) 2C, (c) 3C, and (d) 5C discharge rates.

Two key parameters were considered to more accurately evaluate the thermal management improvement using the fin-enhanced PCM-based BTMSs compared to the PCM cooling system without fins at high discharge rates of 3C and 5C. These parameters were the fin efficiency and the overall fin effectiveness. The fin efficiency was defined as the ratio of the actual heat transfer rate to the ideal heat transfer rate from the fin, assuming the entire fin was at the temperature of the fin base. The overall fin effectiveness was calculated as the ratio of the total heat transfer from the finned surface to that from the same surface but without fins [55]. Fig. 10 (a) and (b) show the fin efficiency and the overall fin effectiveness, respectively, in the fin-enhanced PCM-based BTMSs with different fin quantities compared to the PCM cooling system without fins at the end of the 3C and 5C discharge rates. The fin efficiency and the overall fin effectiveness of the fin-enhanced PCM-based BTMSs were significantly influenced by the battery heat generation level. As the discharge rate increased, the fin efficiency and the overall fin effectiveness in all BTMSs increased. Specifically, in the PCM-based BTMS with 4 internal-external fins, the values for the fin efficiency were 0.236 and 0.378 at the end of the 3C and 5C discharge rates, respectively. However, when the fin quantity was increased from 4 to 12, the fin efficiency decreased by 29.30% and 32.79% at the end of the 3C and 5C discharge rates, respectively. This reduction in the fin efficiency was due to the higher temperature difference between the base of the fin and its tip in the systems with a greater number of fins. Indeed, the increased fin quantity resulted in the generated heat being

distributed among a larger quantity of fins, reducing the fin efficiency. However, there was an insignificant increase in the overall fin effectiveness by increasing the fin quantity from 4 to 12, with a maximum rise of 1.08% at the end of the 5C discharge rate. Hence, it can be concluded that the BTMS with 4 internal-external fins provided the highest fin efficiency and remained competitive in overall fin effectiveness compared to the BTMSs with greater fin quantities.

Fig. 10 (c) and (d) also compare the heat storage rate and heat dissipation rate, respectively, in the PCM-based BTMSs with different fin quantities at the end of the 3C and 5C discharge rates. Compared to the heat dissipation rate, a considerable proportion of the generated heat was stored in the PCM-based BTMSs. Furthermore, increasing the discharge rate led to a greater increase in the heat storage rate compared to the heat dissipation rate in all PCM-based BTMSs due to the absorption of a higher amount of heat, generated at the higher discharge rate, by the PCM. When the fin quantity was increased from 0 to 12, the heat dissipation rate increased by 0.577 and 0.740 W at the end of the 3C and 5C discharge rates, respectively, due to the enhanced heat transfer area. This increase in the heat dissipation rate was achieved at the cost of the reduced heat storage rate. At the end of the 3C and 5C discharge rates, the BTMS with 4 internal-external fins achieved a heat storage rate that was 0.92 and 0.96 of that in the PCM cooling system without fins, respectively. However, the heat dissipation rate in the BTMS with 4 internal-external fins was 1.82 and 2.10 times greater than that in the PCM cooling system without fins at the end of the 3C and 5C discharge
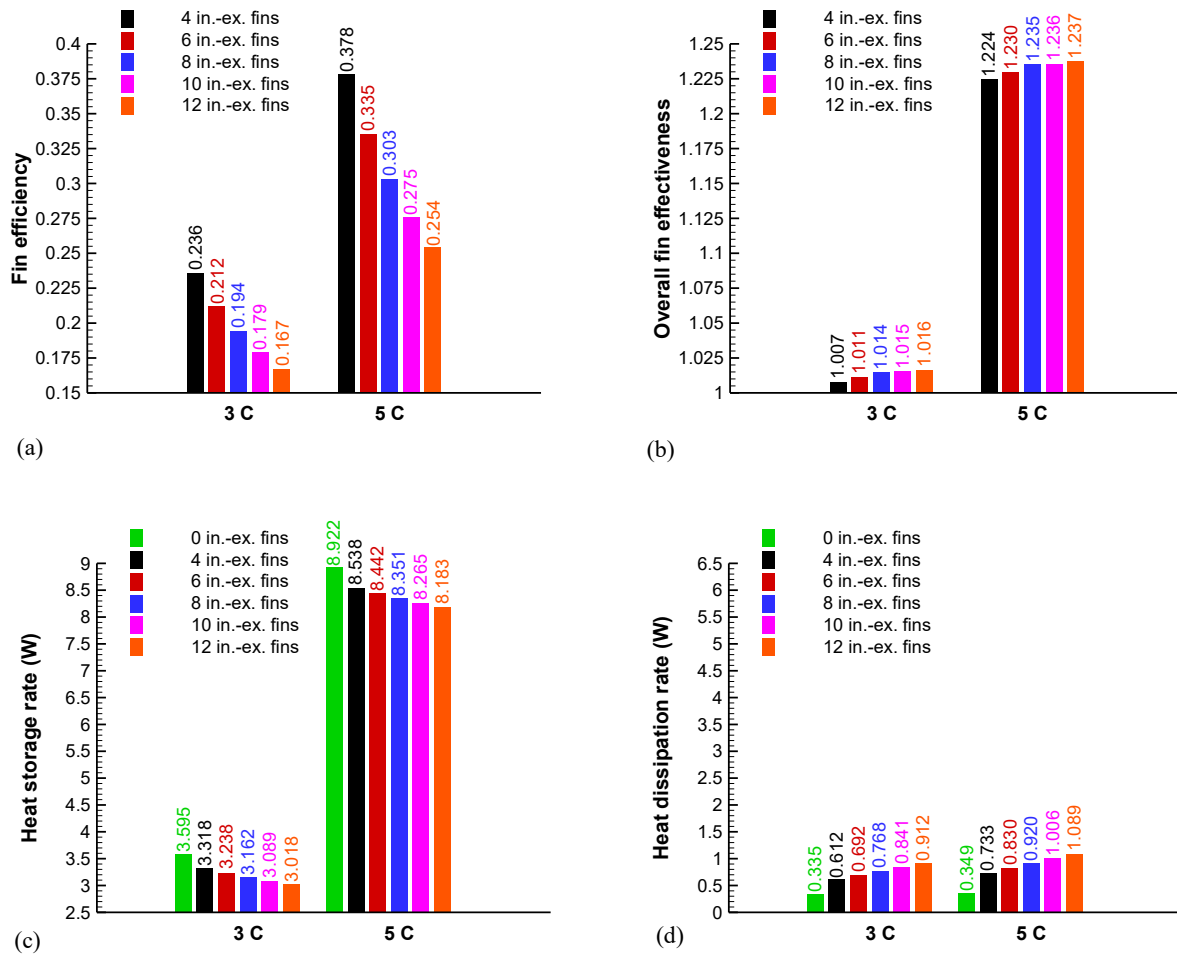
Fig. 10. (a) The fin efficiency, (b) the overall fin effectiveness, (c) heat storage rate, and (d) heat dissipation rate in the PCM-based BTMSs with different fin quantities at the end of the 3C and 5C discharge rates.

rates, respectively. Therefore, the PCM-based BTMS with 4 internal-external fins provided a balance between the heat storage rate and heat dissipation rate, effectively utilising the sensible and latent heat capacity of the PCM and natural convection heat transfer to the surrounding environment.

Fig. 11 shows the contour plots for the temperature and PCM liquid fraction at the middle height of the BTMSs with different fin quantities under transient heat generation of the battery at 5C discharge rate and t = 720 s. In the PCM cooling system without fins, the PCM was melted entirely around the battery surface, and the heat was trapped within the liquid PCM around the battery surface due to the poor thermal conductivity of the PCM. However, in the fin-enhanced PCM-based BTMSs, the liquid fraction distributions concretely reflected that the PCM silos around the battery created by the internal-external fins more uniformly exploited the latent heat of the PCM all around each PCM silo compared to the PCM cooling system without fins. Hence, a noticeable difference in the temperature contour plots was observed when the number of fins increased from 0 to 4, which indicated the temperature reduction on the surface and in the central area of the battery in the fin-enhanced PCM-based BTMSs compared to the PCM cooling system without fins. When the fin quantity further increased, external fins slightly enhanced heat dissipation to the surroundings, thus further slowing down the PCM melting process, and a slight change in the temperature distributions was detected. These results highlighted the effectiveness of combining internal-external fins with the PCM cooling system to prevent heat accumulation around the battery surface, efficiently exploit the PCM heat storage capacity, and enhance the thermal management performance of the PCM-based BTMS.

While the increase in the number of internal-external fins could extend the heat transfer area within the PCM and heat transfer area to the surrounding environment, it would reduce the PCM volume and increase the cost and weight of the BTMS. This reduction in the PCM volume decreases the heat storage capacity of the PCM in the BTMS. The increase in the BTMS weight could also reduce the energy density of the system, which can be calculated as [56]:

$$E_d = \frac{UC_0}{m} \tag{19}$$

where E_d, U, C_0, and m stand for the energy density, battery nominal voltage, battery nominal capacity, and BTMS mass, respectively. Therefore, achieving an optimum fin quantity is vital to decrease the battery temperature, enhancing PCM heat storage capacity, increasing energy density, and reducing the cost of manufacturing.

Fig. 12 compares the PCM-based BTMSs with different fin quantities regarding their thermal management performance, energy density, and PCM volume. Fig. 12(a) presents the average values for the maximum temperature on the battery surface in these BTMSs during various discharge rates. It can be observed that there was an insignificant reduction in the average temperature by increasing the fin quantity during all discharge rates, with a maximum reduction of 0.19%. Admittedly, adding fin quantity leads to an increase in the total mass of the system due to the higher density of aluminium alloy compared to that of PCM. Fig. 12(b) shows an almost linear declining trend in the energy density of the system by increasing the fin quantity owing to the
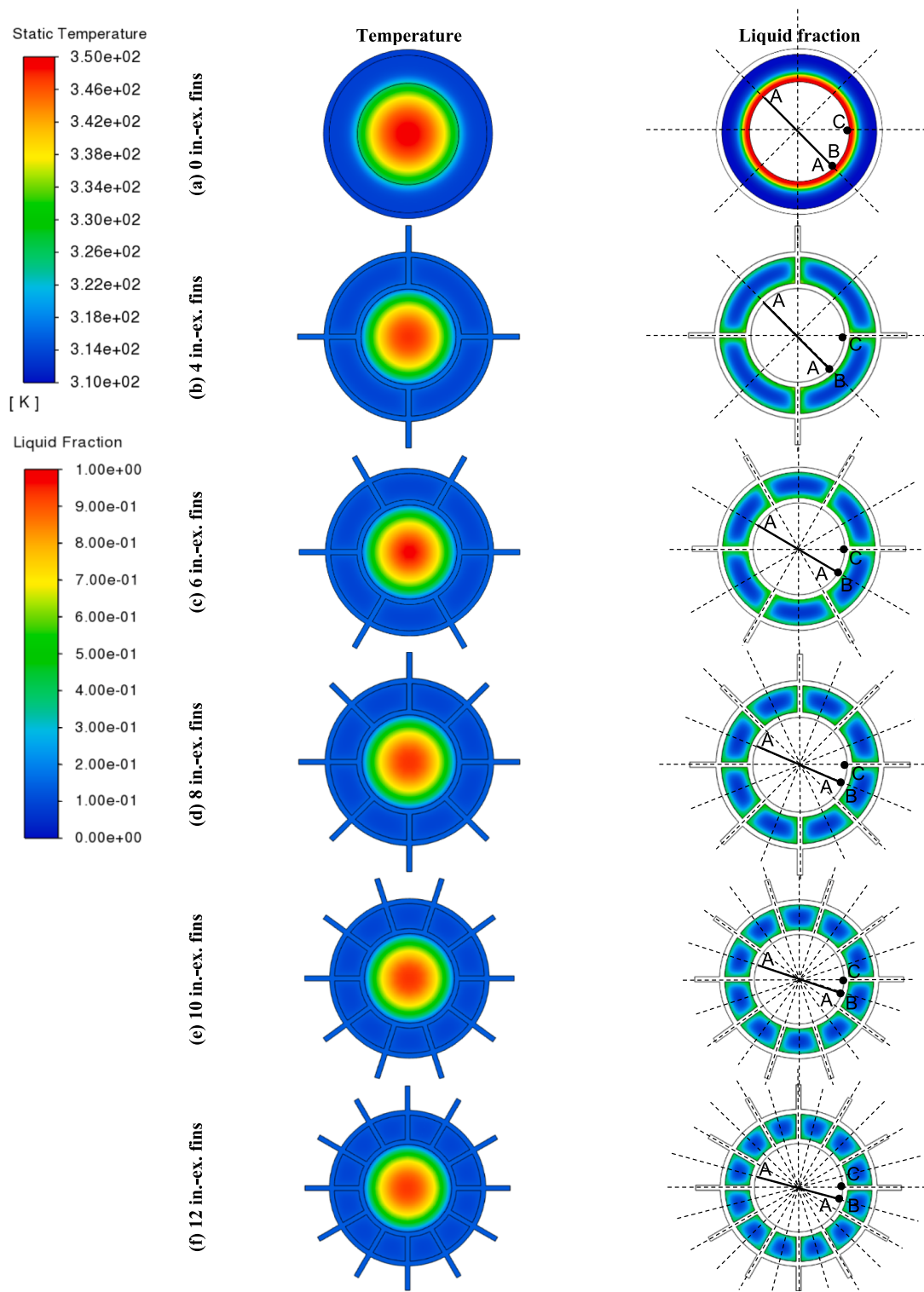
Fig. 11. Comparison of the temperature and PCM liquid fraction distributions at the middle height of the BTMSs with various fin quantities at the end of the 5C discharge rate (the dashed lines show the symmetry planes).

increase in the system mass, decreasing the energy density by 2.71%, 5.27%, 7.71%, and 10.02% in the BTMSs with 6, 8, 10, and 12 internal-external fins compared to the BTMS with 4 internal-external fins, respectively. As shown in Fig. 12(c), the PCM volume decreased by 2.90%, 5.80%, 8.21%, and 11.11% in the BTMSs with 6, 8, 10, and 12 fins compared to the BTMS with 4 fins, respectively. Therefore, 4 internal-external fins were an optimum fin quantity for the developed

BTMS, which effectively conducted the thermal management and promoted the thermal safety for the battery while providing the energy density of the system and the PCM volume at a higher level compared to the greater fin quantities.

The temperature drop was calculated for two cases as the difference in the average value of the maximum temperature on the battery surface during various discharge rates between the fin-enhanced PCM-based
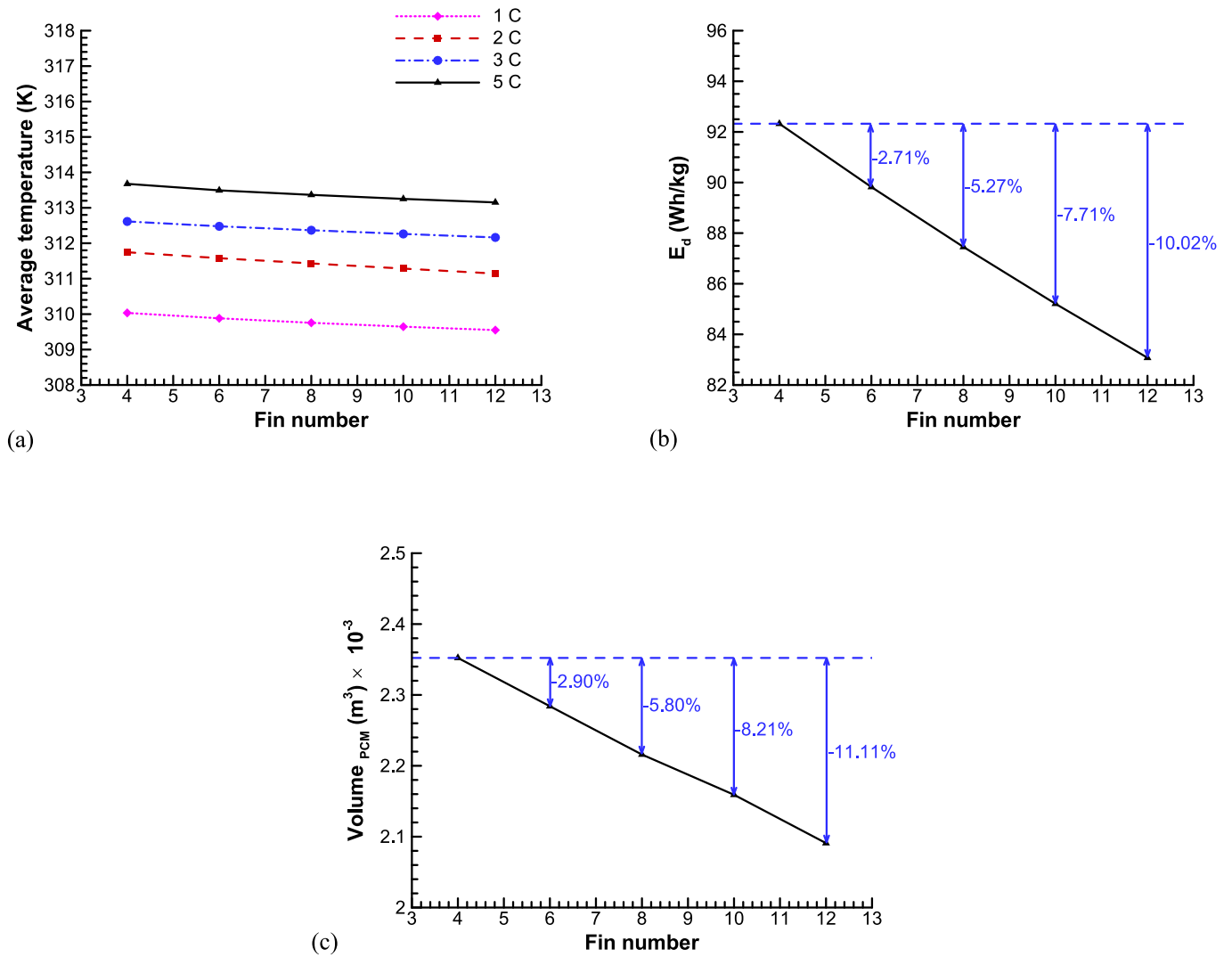
Fig. 12. Comparison of (a) the average of the maximum temperature on the battery surface at 1C, 2C, 3C, and 5C discharge rates, (b) the energy density of the systems, and (c) the PCM volume in the BTMSs with different number of internal-external fins.
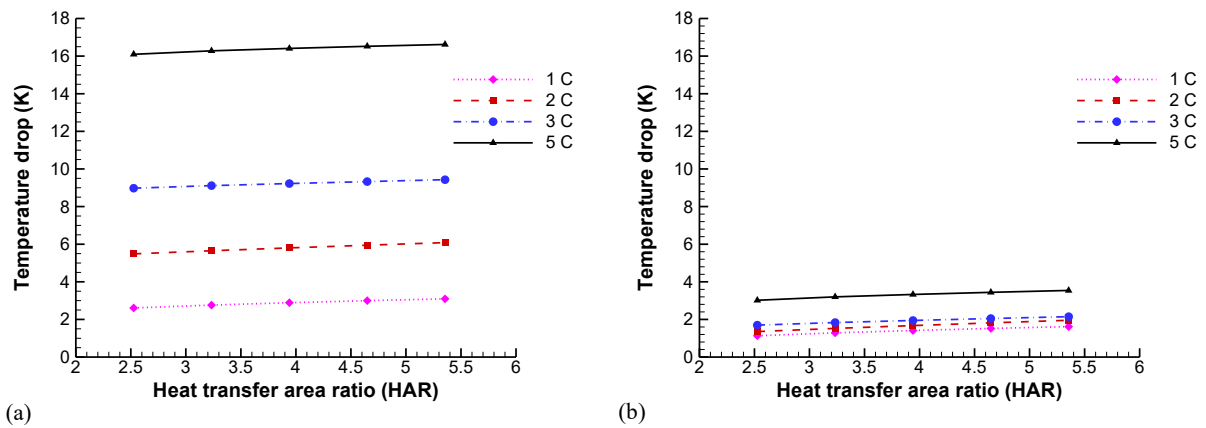

Fig. 13. The temperature drop vs HAR in the PCM-based BTMSs with different fin quantities compared to (a) the battery system with natural air convection cooling and (b) the PCM cooling system without fins at various discharge rates.

BTMSs and the battery system with natural air convection cooling (case 1), as shown in Fig. 13 (a), and between the fin-enhanced PCM-based BTMSs and the PCM cooling system without fins (case 2), as shown in Fig. 13 (b). The heat transfer area ratio (HAR) was also defined as the

ratio of the surface heat transfer area of the system with fins to that of the system without fins [57]. The corresponding HARs in the PCM-based BTMSs with 4, 6, 8, 10, and 12 internal-external fins were 2.53, 3.23, 3.94, 4.65, and 5.35, respectively. The temperature drop in both cases

increased by increasing the discharge rate, emphasising the effectiveness of the fin-enhanced PCM-based BTMSs, especially at the 5C discharge rate, which is a harsh condition with a large amount of battery heat generation. Indeed, the BTMS with 4 internal-external fins achieved a 16.1 and 2.95 K reduction in the average temperature compared to the battery system with natural air convection cooling and PCM cooling system without fins at the high discharge rate of 5C and high ambient temperature of 308.15 K. However, the temperature drop enhanced slightly as the HAR value increased. Therefore, the beneficial effects of the proposed internal-external fins on the thermal management performance improved negligibly, even by increasing the HAR value to more than double from 2.53 to 5.35. Therefore, these results again highlighted that 4 internal-external fins were sufficient for the developed BTMS.

The thermal performance of the BTMSs with various fin quantities was also investigated under constant heat generation of the battery at 3C and 5C discharge rates until PCM was melted entirely, as shown in Fig. 14. At the beginning of the 3C and 5C discharge rates, the maximum temperature on the battery surface increased quickly in all systems, exploiting the PCM sensible heat capacity. The improved conductive heat transfer within the PCM through the internal fins and enhanced natural convective heat transfer to the surroundings through the external fins resulted in the lower maximum temperature in the fin-enhanced PCM-based BTMSs compared to the PCM cooling system without fins. During the PCM sensible heat storage, increasing the fin quantity in the fin-enhanced PCM-based BTMSs reduced the temperature rise rate at the 3C discharge rate and showed an insignificant effect on the maximum temperature at the 5C discharge rate. These negligible differences in the maximum temperature in the fin-enhanced PCM-based BTMSs with various fin quantities can be attributed to the high heat generation of the battery at the 5C discharge rate that extending the heat transfer area during the PCM sensible heat storage did not enhance heat dissipation. Then, the temperature rise rate significantly decreased above the PCM solidus temperature of 313.75 K at 3C and 5C discharge rates, indicating that the PCM melting process was triggered. This reduction in the maximum temperature was more pronounced in the fin-enhanced PCM-based BTMSs compared to the PCM cooling system without fins, highlighting the prominent role of the fins in effectively exploiting the PCM latent heat capacity by increasing the heat conducting paths within the PCM. An increment in the number of longitudinal internal-external fins contributed to the enlargement of the heat transfer area to utilise the PCM latent heat capacity, which reduced the maximum temperature. At the end of the complete melting of the PCM, an upward trend in the maximum temperature curves was also detected since the latent heat capacity of the PCM was almost entirely employed, and the heat was trapped within the melted PCM, especially at the 5C

discharge rate with a higher level of the battery heat generation. When the PCM was completely melted, the maximum temperature in the PCM-based BTMSs with 4, 6, 8, 10, and 12 internal-external fins reduced by 9.90 (3%), 10.46 (3.17%), 10.96 (3.32%), 11.38 (3.45%), and 11.72 K (3.55%) at 3C discharge rate and by 17.45 (5.10%), 18.05 (5.28%), 18.97 (5.55%), 19.88 (5.81%), and 20.67 (6.04%) K at 5C discharge rate compared to the PCM cooling system without fins, respectively. Therefore, the PCM-based BTMSs with longitudinal internal-external fins effectively controlled the maximum temperature below 325 K, even at the high discharge rate of 5C.

Fig. 15 (a) and (b) present the variations in the PCM liquid fraction over time in the PCM-based BTMSs with various quantities of internal-external fins until the PCM was completely melted. Fig. 15 (c) and (d) also show more details about when the PCM melting process started and ended and the PCM melting period. The beginning of the PCM melting process was delayed by increasing the fin quantity. While the generated heat was conducted and distributed in the fin-enhanced PCM-based BTMSs through the cylindrical and longitudinal internal fins, it was dissipated to the surroundings through the external fins and housing. Therefore, these internal-external fins increased the time required for the PCM to reach its melting temperature. This delay in the onset of the PCM melting process was less significant at the 5C discharge rate due to the higher level of the battery heat generation that dissipated more slowly to the surroundings.

At the 3C discharge rate, the BTMSs with 4, 6, 8, 10, and 12 internal-external fins prolonged the PCM melting period by 33.20%, 53.80%, 84.26%, 135.66%, and 246.54% compared to the PCM cooling system without fins, respectively. While there was less PCM volume to be melted in the BTMSs with greater fin quantities, increasing the number of internal-external fins lengthened the PCM melting period due to the increased heat transfer area to the surroundings through the external fins that decreased the PCM temperature. Therefore, the contribution of the convective heat transfer to the surroundings in prolonging the PCM melting period through external fins outweighed the share of the enhanced heat conduction within the systems in accelerating the PCM melting process through internal fins. At the 5C discharge rate, the BTMSs with 4, 6, and 8 internal-external fins shortened the PCM melting period by 3.34%, 1.25%, and 0.34% compared to the PCM cooling system without fins, respectively. However, the BTMSs with 10 and 12 internal-external fins lengthened the PCM melting period by 0.53% and 1.65%, respectively, compared to the PCM cooling system without fins. The high heat generated within the battery at the 5C discharge rate was transferred to the PCM through heat-conducting internal-external fins, thus melting the PCM more rapidly in the BTMSs with 4, 6, and 8 internal-external fins compared to the PCM cooling system without fins. However, greater quantities of internal-external fins slightly increased
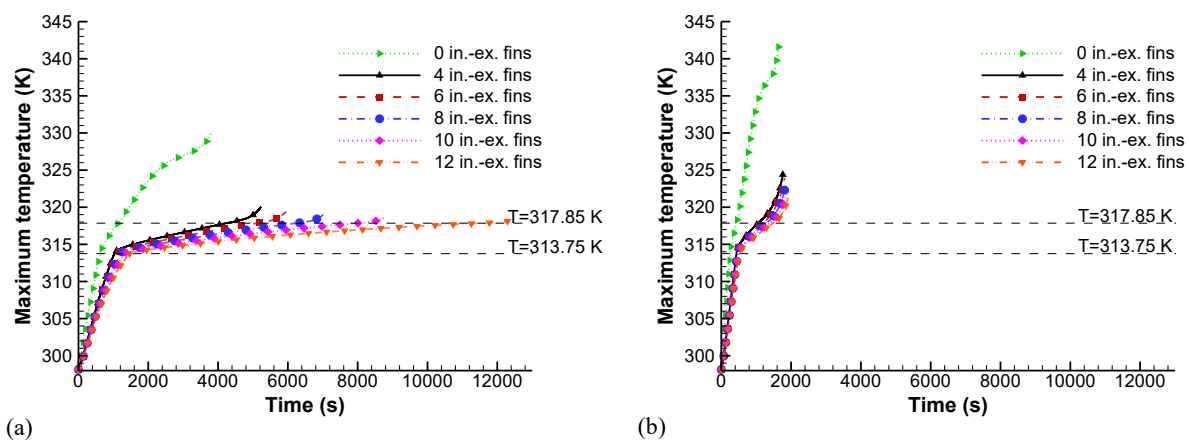

Fig. 14. Variation of the maximum temperature on the battery surface in the PCM-based BTMSs with different fin quantities under constant heat generation of the battery at the (a) 3C and (b) 5C discharge rates.
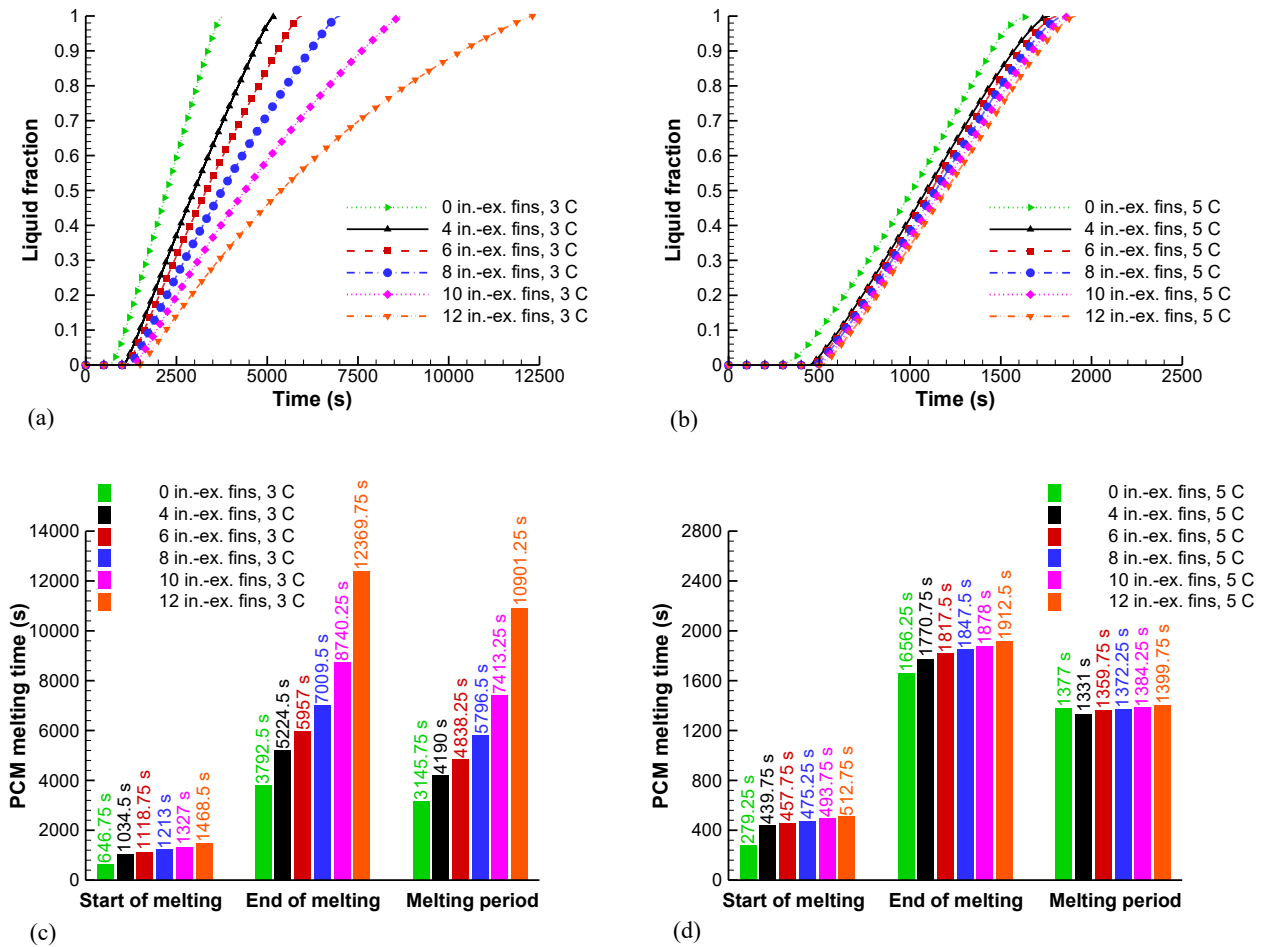
Fig. 15. Variation of PCM liquid fraction in the PCM-based BTMSs with different fin quantities under constant heat generation of the battery at (a) 3C and (b) 5C discharge rates and the PCM melting time at (c) 3C and (d) 5C discharge rates.

the PCM melting period, which indicated the dominant role of the improved convective heat transfer to the surroundings through external fins in prolonging the PCM melting period compared to the effect of the enhanced conductive heat transfer within the PCM on decreasing the PCM melting period at the 5C discharge rate. While increasing the number of fins significantly lengthened the PCM melting period, hence increasing the period that the battery temperature was in the safe range at the discharge rate of 3C, there must be a trade-off among the system's energy density, PCM heat storage capacity, thermal performance, and PCM melting period. As discussed above, 4 internal-external fins were sufficient for conducting the heat generated within the battery to the PCM and dissipating heat to the surroundings through natural air convection while providing higher energy density and PCM heat storage capacity compared to the greater fin quantities and controlling the battery temperature for an appropriate period.

Since it is essential to have a uniform temperature distribution in a single battery cell, the temperature profiles in the BTMSs should be investigated, which has not been reported in previous studies on BTMSs. Fig. 16 illustrates the temperature profiles on a line at the intersection of a plane at the middle height of the battery and A-A vertical plane, shown in Fig. 11, and along the battery height on B-B and C–C vertical lines at t = 600 s and t = 1500 s in the PCM-based BTMSs with different fin quantities under constant heat generation of the battery at the 5C discharge rate. Fig. 11 shows the position of point B and point C on the symmetry planes that created B-B and C–C lines, respectively, on the battery surface and along the battery height in the Y-direction. As shown in Fig. 16 (a), after 600 s, the temperature at the centre of the battery in the BTMSs with 4, 6, 8, 10, and 12 internal-external fins decreased by

3.53, 2.22, 4.07, 4.28, and 4.71 K compared to the PCM cooling system without fins, respectively. Furthermore, after 1500 s, the temperature at the centre of the battery in the BTMSs with 4, 6, 8, 10, and 12 fins decreased by 11.53, 9.32, 12.42, 12.68, and 13.19 K compared to the PCM cooling system without fins, respectively. The higher battery temperature in the PCM cooling system without fins compared to that in the fin-enhanced PCM-based BTMSs can be attributed to the heat accumulation in the liquid PCM around the battery surface due to the low thermal conductivity of the PCM. This heat accumulation in the PCM cooling system without fins increased at t = 1500 s, leading to more significant differences in the temperature profiles between the PCM cooling system without fins and fin-enhanced PCM-based BTMSs. Therefore, the proposed internal-external fins effectively reduced the temperature on the surface and at the centre of the battery. Increasing the fin quantity in the fin-enhanced PCM-based BTMSs gradually decreased the temperature at the middle height of the battery. However, there was an increase in the temperature at the centre of the battery when the fin quantity increased from 4 to 6, indicating that the contribution of the increased heat transfer area and the position of fins in the BTMS with 6 fins in penetrating the BTMS's cooling effect into the centre of the battery was dominated by the high heat generated at the 5C discharge rate.

As shown in Fig. 16 (c) and (d), almost uniform temperature distributions along the height of the battery were achieved in the PCM-based BTMSs with internal-external fins compared to the PCM cooling system without fins. In the PCM cooling system without fins, the battery was in direct contact with the PCM. The top of the PCM covering the battery surface was more quickly melted than the bottom of the PCM due to the
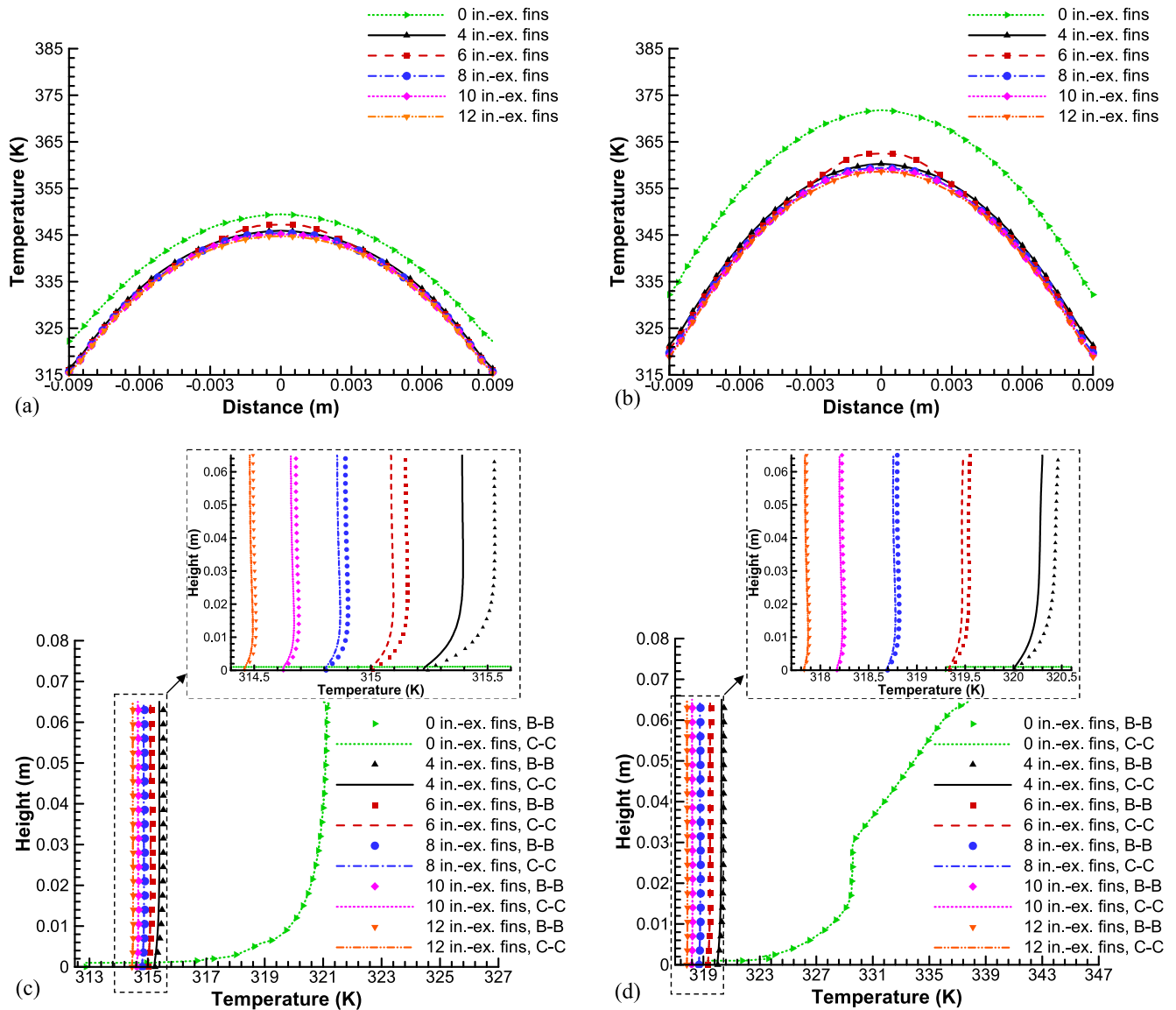
Fig. 16. Temperature profiles at the middle height of the battery on A-A planes at (a) t = 600 s and (b) t = 1500 s and along the height of the battery on B-B and C–C lines at (c) t = 600 s and (d) t = 1500 s in the PCM-based BTMSs with different fin quantities under constant heat generation of the battery at 5C discharge rate.

buoyance-driven natural convection within the PCM that carried the melted PCM toward the top of the PCM silo. Sun, et al. [27] also reported similar non-uniform PCM melting in a cylindrical housing. Therefore, the temperature on the top of the battery surface was higher than the bottom due to the accumulated heat in the liquid PCM. This temperature gradient between the top and bottom of the battery in the PCM cooling system without fins was more significant at t = 1500 s compared to t = 600 s because of the higher PCM liquid fraction and higher accumulated heat in the liquid PCM. Increasing the fin quantity in the PCM-based BTMSs with internal-external fins slightly decreased the temperature gradient on the B-B and C–C lines. These more uniform temperature distributions can be attributed to the enhanced conduction within the systems and improved convection heat transfer to the surroundings. Furthermore, the temperature on the C–C lines in the fin-enhanced PCM-based BTMSs was slightly lower than that on the B-B lines because of the shorter distance of the C–C lines to the fins exposed to the ambient temperature. These differences in the temperature profiles around the circular perimeter of the battery on the B-B and C–C lines were reduced by increasing the fin quantity due to the shorter distance between these two lines. Therefore, the PCM-based BTMS with 4 internal-external fins

provided an almost uniform cooling effect around the circular perimeter and along the height of the battery compared to the PCM cooling system without fins.

5.3. Non-dimensional analysis and correlations for liquid fraction and Nusselt number

Nusselt number can be utilised to characterise the heat transfer mechanisms governing the PCM melting process [58]. It is worth noting that all the non-dimensional parameters used in this study were calculated when the surface-averaged temperature of the fin and the housing around the PCM silos was higher than the PCM melting temperature. The surface-averaged Nusselt number ($\overline{Nu}$) is expressed as [57,59]:

$$\overline{Nu}(t) = \frac{\overline{h}(t)H}{k_l} \tag{20}$$

where $\overline{h}$ is the surface-averaged heat transfer coefficient, H is the characteristic length, which is the BTMS height, and k_l is the thermal conductivity of the liquid PCM. In addition, $\overline{h}$ can be obtained by [57,59]:

$$\overline{h}(t) = \frac{Q_t(t)}{A_w(T_w - T_m)\Delta t} \qquad (21)$$

where $Q_t(t)$ is the instantaneous total heat absorbed by the PCM during the time interval of Δt, A_w is the total heat transfer area, including the housing and fin surface in contact with the PCM, T_w is the transient surface-averaged temperature of the fin and the housing around the PCM, and T_m is the PCM melting temperature.

Since Fourier number (*Fo*) alone is not sufficient to convey the generalised trend of the heat transfer variation due to the effect of the phase change process, the dimensionless time (τ) that takes into account the transient heat conduction and PCM phase change is defined as [57,59]:

$$\tau = Fo \times Ste^* \qquad (22)$$

where Ste^* is the modified Stefan number, which includes the sensible heat of the solid and liquid phases of the PCM. Fig. 17 presents the variation of the surface-averaged Nusselt number versus the dimensionless time in the fin-enhanced PCM-based BTMSs with various numbers of internal-external fins at 3C and 5C discharge rates until the PCM was completely melted. Based on the Nusselt number definition, which is the ratio of the convective to conductive heat transfer, the heat transfer mechanisms of the PCM melting process were approximately divided into the conduction regime, the strong convection regime, and the weak convection regime. First, the PCM melting process started with the conduction heat transfer. Then, the effect of natural convection increased up to a certain time. After that, the impact of natural convection diminished towards the end of the PCM complete melting process. These subdivisions of heat transfer mechanisms were also reported for thermal energy storage systems [60], heat sinks [59], and thermal reservoirs [61] but not for BTMS.

During the heat conduction regime, the heat transfer within the PCM occurred only due to the conduction effects. The high value of the Nusselt number at the beginning of the PCM melting process could be attributed to the low thermal resistance of the extremely thin liquid PCM layer. As the PCM melting process progressed, the liquid PCM layer became thicker, which increased the thermal resistance, thus sharply decreasing the Nusselt number from its peak value. Increasing the fin quantity marginally decreased the Nusselt number during this heat conduction regime due to the increased heat transfer area.

During the strong convection regime, the dominant natural convection heat transfer within the PCM intensified the heat transfer. While the thermal resistance increased as more PCM melted, strong convection enhanced the heat transfer rate due to the increased intensity of the liquid PCM flow. Therefore, the Nusselt number decreased at a slower rate. The Nusselt number had higher values in the BTMSs with fewer fins, which can be due to the larger melting rate of PCM and stronger natural convection regions in the PCM silos in the BTMSs with fewer fins. These differences in the Nusselt number values were less significant at the 5C discharge rate with higher battery heat generation due to the smaller differences in the PCM melting rate and natural convection heat transfer within the melted PCM in the BTMSs with various fin quantities compared to the 3C discharge rate.

During the weak convection regime, the Nusselt number decreased and had very low values compared to the other two heat transfer regimes. The low value of the Nusselt number indicated that the heat transfer rate in the BTMSs decreased because of the weak natural convection, thus increasing the battery temperature at the end of the PCM melting process.

Therefore, the PCM-based BTMS with 4 internal-external fins was appropriate to take advantage of natural convection and conduction heat transfer within the PCM to control the battery temperature.

It is also beneficial to correlate with the PCM liquid fraction and Nusselt number, which can be used for various fin quantities and discharge rates. While the non-linearity of the liquid fraction and Nusselt number evolution, their dependency on many parameters, and transient heat flux on the walls in the BTMSs made it challenging to develop these correlations, the present work developed correlations for the PCM liquid fraction and surface-averaged Nusselt number. The intensity of the natural convection during the melting process is also quantified by the Rayleigh number (*Ra*), which is defined as [57]:

$$Ra = \frac{g\beta(T_w - T_m)H^3}{v\alpha} \qquad (23)$$

where v is the kinematic viscosity, and α is the thermal diffusivity of liquid PCM. Fig. 18 (a) and (b) show the PCM liquid fraction and the corresponding ratio of the surface-averaged Nusselt number to Rayleigh number curves versus an appropriate combination of the Fourier number, modified Stefan number, Rayleigh number, and fin quantity, N, as well as the fitting curves at 3C and 5C discharge rates, respectively. The exponents of *Fo*, Ste^*, *Ra*, and $(1 + N)$ were determined from a least-squares fit to all the data for the PCM liquid fraction and Nusselt number. Consequently, nonlinear regression analyses were conducted for curve fitting the data for the liquid fraction and Nusselt number as:

$$\gamma = 4.0972 \times 10^{-7} \times X^{15.3144} - 4.5968 \times 10^{-7} \times X^{15.1931} \qquad (24)$$
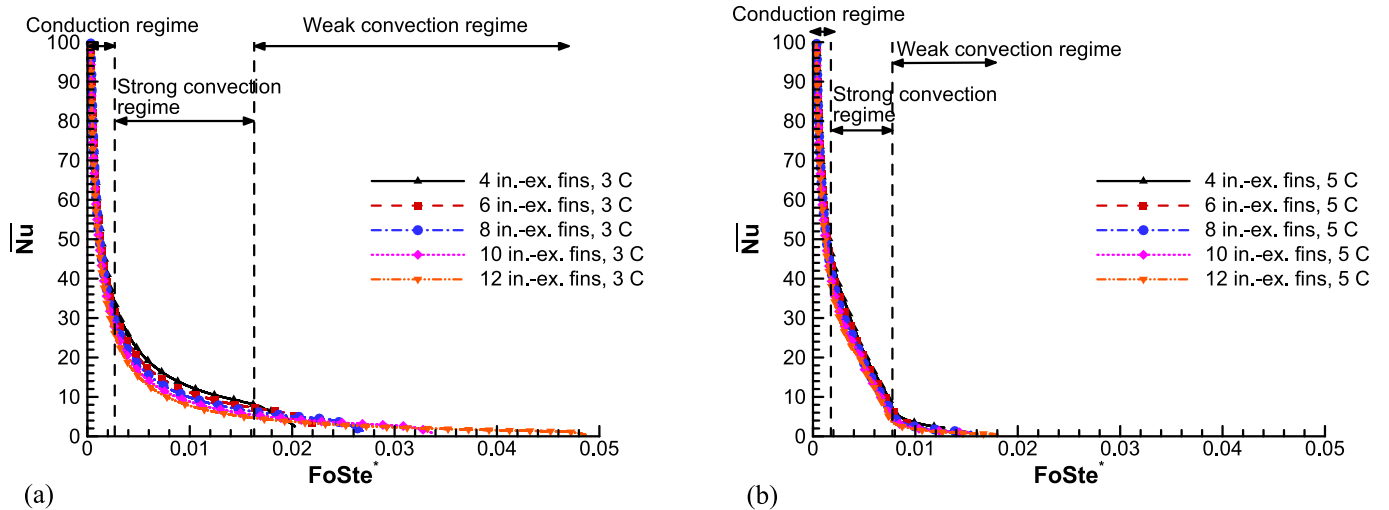

Fig. 17. Variation of the surface-averaged Nusselt number vs the dimensionless time in the PCM-based BTMSs with various quantities of internal-external fins at (a) 3C and (b) 5C discharge rates.
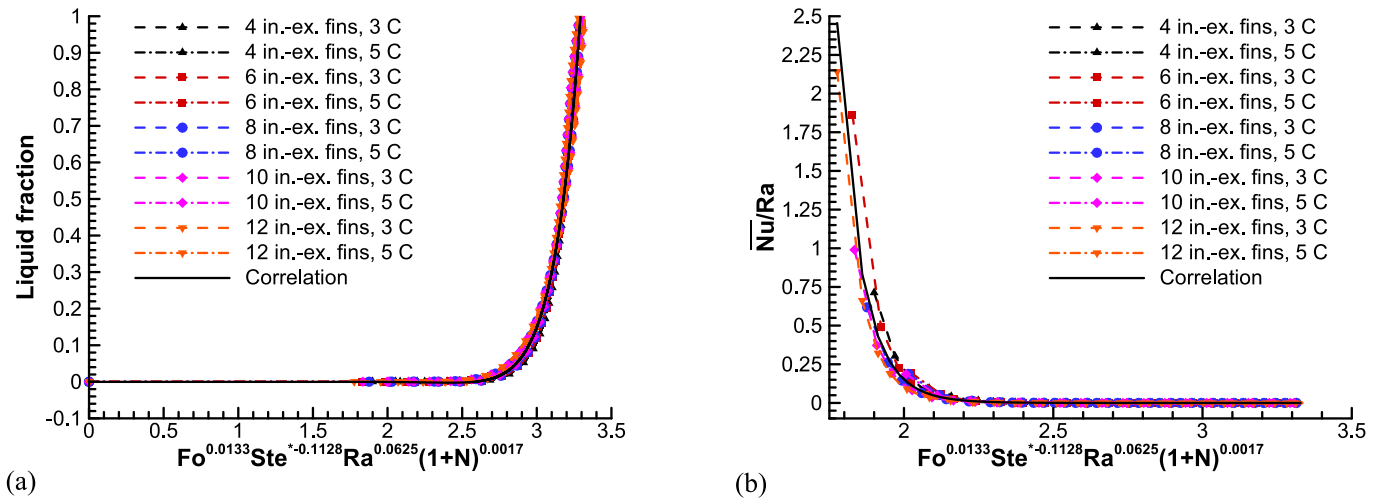
Fig. 18. Generalised results for (a) the PCM liquid fraction and (b) the ratio of the surface-averaged Nusselt number to Rayleigh number in the BTMSs with different fin quantities at 3C and 5C discharge rates.

$$\frac{\overline{Nu}}{Ra} = 1.96 \times 10^{-6} + 1.74 \times 10^6 \times X^{-23.45} \tag{25}$$

$$X = Fo^{0.0133}Ste^{*-0.1128}Ra^{0.0625}(1+N)^{0.0017} \tag{26}$$

The ranges of the parameters in the above correlations were as follows: $0 < Fo \leq 0.2820$; $0.1296 \leq Ste^* \leq 0.3285$; $1.5997 \times 10^2 \leq Ra \leq 5.3159 \times 10^7$; and $4 \leq N \leq 12$.

The R-square values were 95.3% and 94.4% for the PCM liquid fraction and the ratio of Nusselt number to Rayleigh number, respectively, showing that the correlations had good accuracy. During the natural convection in the PCM, the Rayleigh number showed laminar flow (less than 10^9); hence no turbulence model was considered.

6. Conclusion

Thermal management systems must be carefully designed for electric vehicles to ensure lithium-ion batteries operate safely, prolong batteries' lifespan, and prevent thermal runaway of the batteries. This study proposed a PCM-based BTMS with cylindrical and longitudinal internal-external fins within a metal housing, creating PCM silos around the cylindrical battery. The effectiveness of the proposed BTMS was explored during transient heat generation of the battery at various discharge rates of 1C, 2C, 3C, and 5C and constant heat generation of the battery at high discharge rates of 3C and 5C. The effects of fin quantity on thermal management performance, energy density, heat storage capacity, and PCM melting time were evaluated. Furthermore, the thermal performance of the developed BTMS was compared to that of the battery system with natural air convection cooling and the PCM cooling system without fins. The following conclusions can be made:

(1) The cylindrical and longitudinal internal-external fins around the battery surface acted as conductive and convective heat transfer enhancers within the PCM, increased the heat transfer area to dissipate heat to the surroundings, and extended the period that the PCM latent heat was exploited, thus maintaining the battery temperature in a safe temperature range for a longer period compared to the PCM cooling system without fins.

(2) In contrast to the battery system with natural air convection cooling and the PCM cooling system without fins, the PCM-based BTMS with internal-external fins effectively maintained the battery surface temperature well below the optimum temperature of 318.15 K for the battery safety and lifespan under transient heat generation of the battery, even at the high discharge rate of 5C and high ambient temperature of 308.15 K.

(3) At the end of the PCM complete melting process, the BTMS with 4 internal-external fins decreased the battery surface temperature by 9.90 and 17.45 K compared to the PCM cooling system without fins at the discharge rates of 3C and 5C, respectively.

(4) The BTMS with 4 internal-external fins provided the highest fin efficiency and remained competitive in the overall fin effectiveness compared to the BTMSs with greater fin quantities, providing the fin efficiency of 0.378 and the overall fin effectiveness of 1.224 at the end of the 5C discharge rate.

(5) The BTMS with 4 internal-external fins effectively utilised the sensible and latent heat capacity of the PCM and natural convection heat transfer to the surroundings by providing a heat storage rate 0.92 and 0.96 times that of the PCM cooling system without fins at the end of the 3C and 5C discharge rates, respectively. It also achieved a heat dissipation rate 1.82 and 2.10 times that of the PCM cooling system without fins at the end of the 3C and 5C discharge rates, respectively.

(6) In the fin-enhanced PCM-based BTMS, 4 internal-external fins were an optimum fin quantity to effectively conduct the battery thermal management while providing up to 10.02% higher energy density and 11.11% higher heat storage capacity than the greater fin quantities.

(7) The proposed PCM-based BTMS with 4 internal-external fins provided an almost uniform cooling effect around the circular perimeter and along the height of the battery surface compared to the PCM cooling system without fins.

(8) According to the change in the surface-averaged Nusselt number as a function of the dimensionless time, the heat transfer mechanisms during the PCM melting process in the fin-enhanced PCM-based BTMSs with different fin quantities were divided into conduction heat transfer at the start of the PCM melting process, followed by strong convection heat transfer, and weak convection heat transfer at the end of the PCM melting process.

(9) The PCM liquid fraction and Nusselt number were generalised in terms of a combination of the Fourier number, modified Stefan number, Rayleigh number, and the number of fins. The developed correlations for the PCM liquid fraction and Nusselt number can help researchers design efficient thermal management systems for cylindrical lithium-ion batteries.

Since the external fins have the potential to accelerate the PCM solidification process during the cooling due to the enhanced heat

exchange with the surrounding environment, it is necessary to investigate the reliability of various PCM-based BTMSs during continuous cycles of the PCM complete melting and solidification. The effectiveness of the developed BTMS in a battery pack should be explored. Furthermore, parametric studies should be conducted for the effect of the PCM thickness, fin length, fin thickness, and PCM material to achieve an optimum design for the proposed BTMS. While the proposed system demonstrated promising performance regarding temperature regulation, this research was specifically applicable to cylindrical batteries and may not directly translate to other battery types. Furthermore, the proposed BTMS was efficient under specific transient and constant heat generation conditions and within a particular ambient temperature range. Therefore, the performance of this system should be explored under real driving cycles and broader operating conditions.

Funding

Declaration of Competing Interest

The authors declare that they have no known competing financial interests or personal relationships that could have appeared to influence the work reported in this paper.

Data availability

Data will be made available on request.

References

[1] J.T. Rajan, V.S. Jayapal, M. Krishna, K.M. Firose, S. Vaisakh, A.K. John, A. Suryan, Analysis of battery thermal management system for electric vehicles using 1-Tetradecanol phase change material, Sustainable Energy Technol. Assess. 51 (2022), 101943, https://doi.org/10.1016/j.seta.2021.101943.

[2] S.B. Sanker, R. Baby, Phase change material based thermal management of lithium ion batteries: A review on thermal performance of various thermal conductivity enhancers, J. Storage Mater. 50 (2022), 104606, https://doi.org/10.1016/j.est.2022.104606.

[3] Y. Yang, E.G. Okonkwo, G. Huang, S. Xu, W. Sun, Y. He, On the sustainability of lithium ion battery industry–A review and perspective, Energy Storage Mater. 36 (2021) 186–212, https://doi.org/10.1016/j.ensm.2020.12.019.

[4] A. Nazari, S. Farhad, Heat generation in lithium-ion batteries with different nominal capacities and chemistries, Appl. Therm. Eng. 125 (2017) 1501–1517, https://doi.org/10.1016/j.applthermaleng.2017.07.126.

[5] J. Jaguemont, J. Van Mierlo, A comprehensive review of future thermal management systems for battery-electrified vehicles, J. Storage Mater. 31 (2020), 101551, https://doi.org/10.1016/j.est.2020.101551.

[6] P.A. Sevugan, M. Pradeep, A. Krishnaswamy, K. Karunamurthy, Battery Thermal Management System for electric vehicles using Phase Change Materials, Mater. Today:. Proc. 51 (2022) 1604–1611, https://doi.org/10.1016/j.matpr.2021.10.468.

[7] E. Jiaqiang, M. Yue, J. Chen, H. Zhu, Y. Deng, Y. Zhu, F. Zhang, M. Wen, B. Zhang, S. Kang, Effects of the different air cooling strategies on cooling performance of a lithium-ion battery module with baffle, Appl. Therm. Eng. 144 (2018) 231–241, https://doi.org/10.1016/j.applthermaleng.2018.08.064.

[8] M. Kiani, S. Omiddezyani, E. Houshfar, S.R. Miremadi, M. Ashjaee, A.M. Nejad, Lithium-ion battery thermal management system with Al2O3/AgO/CuO nanofluids and phase change material, Appl. Therm. Eng. 180 (2020), 115840, https://doi.org/10.1016/j.applthermaleng.2020.115840.

[9] Y. Lv, X. Yang, G. Zhang, Durability of phase-change-material module and its relieving effect on battery deterioration during long-term cycles, Appl. Therm. Eng. 179 (2020), 115747, https://doi.org/10.1016/j.applthermaleng.2020.115747.

[10] P.G. Zadeh, Y. Wang, J.D. Chung, Thermal management modeling for cylindrical lithium-ion battery packs considering safety and lifespan, J. Mech. Sci. Technol. 36 (2022) 3727–3733, https://doi.org/10.1007/s12206-022-0646-0.

[11] K. Jiang, G. Liao, E. Jiaqiang, F. Zhang, J. Chen, E. Leng, Thermal management technology of power lithium-ion batteries based on the phase transition of materials: A review, J. Storage Mater. 32 (2020), 101816, https://doi.org/10.1016/j.est.2020.101816.

[12] J. Cao, M. Luo, X. Fang, Z. Ling, Z. Zhang, Liquid cooling with phase change materials for cylindrical Li-ion batteries: An experimental and numerical study, Energy 191 (2020), 116565, https://doi.org/10.1016/j.energy.2019.116565.

[13] N. Ghaeminezhad, Z. Wang, Q. Ouyang, A Review on lithium-ion battery thermal management system techniques: A control-oriented analysis, Appl. Therm. Eng. (2022), 119497, https://doi.org/10.1016/j.applthermaleng.2022.119497.

[14] E.S. Joe, D., Arumuga Perumal, Computational analysis of fluid immersed active cooling for battery thermal management using thermal lattice Boltzmann method, The European Physical Journal Special Topics 231 (2022) 2865–2877.

[15] P. Zare, N. Perera, J. Lahr, R. Hasan, Solid-liquid phase change materials for the battery thermal management systems in electric vehicles and hybrid electric vehicles–A systematic review, J. Storage Mater. 52 (2022), 105026, https://doi.org/10.1016/j.est.2022.105026.

[16] Y. Lv, W. Situ, X. Yang, G. Zhang, Z. Wang, A novel nanosilica-enhanced phase change material with anti-leakage and anti-volume-changes properties for battery thermal management, Energ. Conver. Manage. 163 (2018) 250–259, https://doi.org/10.1016/j.enconman.2018.02.061.

[17] H. Li, X. Liu, G. Fang, Preparation and characteristics of n-nonadecane/cement composites as thermal energy storage materials in buildings, Energ. Buildings 42 (2010) 1661–1665, https://doi.org/10.1016/j.enbuild.2010.04.009.

[18] C. Liu, D. Xu, J. Weng, S. Zhou, W. Li, Y. Wan, S. Jiang, D. Zhou, J. Wang, Q. Huang, Phase Change Materials Application in Battery Thermal Management System: A Review, Materials 13 (2020) 4622, https://doi.org/10.3390/ma13204622.

[19] J.P. Da Cunha, P. Eames, Thermal energy storage for low and medium temperature applications using phase change materials–a review, Appl. Energy 177 (2016) 227–238, https://doi.org/10.1016/j.apenergy.2016.05.097.

[20] S. Landini, J. Leworthy, T. O'Donovan, A review of phase change materials for the thermal management and isothermalisation of lithium-ion cells, J. Storage Mater. 25 (2019), 100887, https://doi.org/10.1016/j.est.2019.100887.

[21] Z. Sun, R. Fan, F. Yan, T. Zhou, N. Zheng, Thermal management of the lithium-ion battery by the composite PCM-Fin structures, Int. J. Heat Mass Transf. 145 (2019), 118739, https://doi.org/10.1016/j.ijheatmasstransfer.2019.118739.

[22] Z.-G. Shen, S. Chen, X. Liu, B. Chen, A review on thermal management performance enhancement of phase change materials for vehicle lithium-ion batteries, Renew. Sustain. Energy Rev. 148 (2021), 111301, https://doi.org/10.1016/j.rser.2021.111301.

[23] V. Choudhari, A. Dhoble, S. Panchal, Numerical analysis of different fin structures in phase change material module for battery thermal management system and its optimization, Int. J. Heat Mass Transf. 163 (2020), 120434, https://doi.org/10.1016/j.ijheatmasstransfer.2020.120434.

[24] J. Weng, Y. He, D. Ouyang, X. Yang, G. Zhang, J. Wang, Thermal performance of PCM and branch-structured fins for cylindrical power battery in a high-temperature environment, Energ. Conver. Manage. 200 (2019), 112106, https://doi.org/10.1016/j.enconman.2019.112106.

[25] J. Weng, D. Ouyang, X. Yang, M. Chen, G. Zhang, J. Wang, Optimization of the internal fin in a phase-change-material module for battery thermal management, Appl. Therm. Eng. 167 (2020), 114698, https://doi.org/10.1016/j.applthermaleng.2019.114698.

[26] H.N. Khaboshan, F. Jaliliantabar, A.A. Abdullah, S. Panchal, Improving the cooling performance of cylindrical lithium-ion battery using three passive methods in a battery thermal management system, Appl. Therm. Eng. (2023), 120320, https://doi.org/10.1016/j.applthermaleng.2023.120320.

[27] Z. Sun, R. Fan, N. Zheng, Thermal management of a simulated battery with the compound use of phase change material and fins: experimental and numerical investigations, Int. J. Therm. Sci. 165 (2021), 106945, https://doi.org/10.1016/j.ijthermalsci.2021.106945.

[28] M.M. Heyhat, S. Mousavi, M. Siavashi, Battery thermal management with thermal energy storage composites of PCM, metal foam, fin and nanoparticle, J. Storage Mater. 28 (2020), 101235, https://doi.org/10.1016/j.est.2020.101235.

[29] Y. Lv, X. Yang, X. Li, G. Zhang, Z. Wang, C. Yang, Experimental study on a novel battery thermal management technology based on low density polyethylene-enhanced composite phase change materials coupled with low fins, Appl. Energy 178 (2016) 376–382, https://doi.org/10.1016/j.apenergy.2016.06.058.

[30] E. Aslan, Y. Aydın, Y. Yaşa, Consideration of graphene material in PCM with aluminum fin structure for improving the battery cooling performance, Int. J. Energy Res. (2022), https://doi.org/10.1002/er.7878.

[31] Y. Wang, T. Gao, L. Zhou, J. Gong, J. Li, A parametric study of a hybrid battery thermal management system that couples PCM with wavy microchannel cold plate, Appl. Therm. Eng. 219 (2023), 119625, https://doi.org/10.1016/j.applthermaleng.2022.119625.

[32] F. Wang, J. Cao, Z. Ling, Z. Zhang, X. Fang, Experimental and simulative investigations on a phase change material nano-emulsion-based liquid cooling thermal management system for a lithium-ion battery pack, Energy 207 (2020), 118215, https://doi.org/10.1016/j.energy.2020.118215.

[33] S. Chen, N. Bao, A. Garg, X. Peng, L. Gao, A fast charging–cooling coupled scheduling method for a liquid cooling-based thermal management system for lithium-ion batteries, Engineering 7 (2021) 1165–1176, https://doi.org/10.1016/j.eng.2020.06.016.

[34] H.M. Barkholtz, A. Fresquez, B.R. Chalamala, S.R. Ferreira, A database for comparative electrochemical performance of commercial 18650-format lithium-ion cells, J. Electrochem. Soc. 164 (2017) A2697, https://doi.org/10.1149/2.1701712jes.

[35] P. Jindal, R. Katiyar, J. Bhattacharya, Evaluation of accuracy for Bernardi equation in estimating heat generation rate for continuous and pulse-discharge protocols in LFP and NMC based Li-ion batteries, Appl. Therm. Eng. 201 (2022), 117794, https://doi.org/10.1016/j.applthermaleng.2021.117794.

[36] Y. Miao, P. Hynan, A. Von Jouanne, A. Yokochi, Current Li-ion battery technologies in electric vehicles and opportunities for advancements, Energies 12 (2019) 1074, https://doi.org/10.3390/en12061074.

[37] H. Wang, T. Tao, J. Xu, X. Mei, X. Liu, P. Gou, Cooling capacity of a novel modular liquid-cooled battery thermal management system for cylindrical lithium ion

batteries, Appl. Therm. Eng. 178 (2020), 115591, https://doi.org/10.1016/j.applthermaleng.2020.115591.

[38] Z. Wang, H. Zhang, X. Xia, Experimental investigation on the thermal behavior of cylindrical battery with composite paraffin and fin structure, Int. J. Heat Mass Transf. 109 (2017) 958–970, https://doi.org/10.1016/j.ijheatmasstransfer.2017.02.057.

[39] N. Zheng, R. Fan, Z. Sun, T. Zhou, Thermal management performance of a fin-enhanced phase change material system for the lithium-ion battery, Int. J. Energy Res. 44 (2020) 7617–7629, https://doi.org/10.1002/er.5494.

[40] R. Fan, N. Zheng, Z. Sun, Evaluation of fin intensified phase change material systems for thermal management of Li-ion battery modules, Int. J. Heat Mass Transf. 166 (2021), 120753, https://doi.org/10.1016/j.ijheatmasstransfer.2020.120753.

[41] H. Yang, H. Zhang, Y. Sui, C. Yang, Numerical analysis and experimental visualization of phase change material melting process for thermal management of cylindrical power battery, Appl. Therm. Eng. 128 (2018) 489–499, https://doi.org/10.1016/j.applthermaleng.2017.09.022.

[42] S. Ambekar, P. Rath, A. Bhattacharya, A novel PCM and TCE based thermal management of battery module, Thermal Science and Engineering Progress 29 (2022), 101196, https://doi.org/10.1016/j.tsep.2022.101196.

[43] J.R. Kermani, M.M. Taheri, M.B. Shafii, A. Moosavi, Analytical solution, optimization and design of a phase change cooling pack for cylindrical lithium-ion batteries, Appl. Therm. Eng. (2023), 120963, https://doi.org/10.1016/j.applthermaleng.2023.120963.

[44] U. Han, H. Choi, H. Lee, H. Lee, Inverse Heat Transfer Analysis Method to Determine the Entropic Coefficient of Reversible Heat in Lithium-Ion Battery, Int. J. Energy Res. 2023 (2023), https://doi.org/10.1155/2023/9929496.

[45] L. Saw, Y. Ye, A. Tay, Electrochemical–thermal analysis of 18650 Lithium Iron Phosphate cell, Energ. Conver. Manage. 75 (2013) 162–174, https://doi.org/10.1016/j.enconman.2013.05.040.

[46] C. Zhao, W. Cao, T. Dong, F. Jiang, Thermal behavior study of discharging/charging cylindrical lithium-ion battery module cooled by channeled liquid flow, Int. J. Heat Mass Transf. 120 (2018) 751–762, https://doi.org/10.1016/j.ijheatmasstransfer.2017.12.083.

[47] H. Huang, H. Wang, J. Gu, Y. Wu, High-dimensional model representation-based global sensitivity analysis and the design of a novel thermal management system for lithium-ion batteries, Energ. Conver. Manage. 190 (2019) 54–72, https://doi.org/10.1016/j.enconman.2019.04.013.

[48] M. Fadl, P.C. Eames, Numerical investigation of the influence of mushy zone parameter Amush on heat transfer characteristics in vertically and horizontally oriented thermal energy storage systems, Appl. Therm. Eng. 151 (2019) 90–99, https://doi.org/10.1016/j.applthermaleng.2019.01.102.

[49] A. Brent, V.R. Voller, K. Reid, Enthalpy-porosity technique for modeling convection-diffusion phase change: application to the melting of a pure metal, Numerical Heat Transfer, Part A Applications 13 (1988) 297–318, https://doi.org/10.1080/10407788808913615.

[50] Y. Hong, W.-B. Ye, J. Du, S.-M. Huang, Solid-liquid phase-change thermal storage and release behaviors in a rectangular cavity under the impacts of mushy region and low gravity, Int. J. Heat Mass Transf. 130 (2019) 1120–1132, https://doi.org/10.1016/j.ijheatmasstransfer.2018.11.024.

[51] T. Sathe, A. Dhoble, Thermal analysis of an inclined heat sink with finned PCM container for solar applications, Int. J. Heat Mass Transf. 144 (2019), 118679, https://doi.org/10.1016/j.ijheatmasstransfer.2019.118679.

[52] S.V. Patankar, Numerical heat transfer and fluid flow, CRC Press, 2018.

[53] F. Chen, R. Huang, C. Wang, X. Yu, H. Liu, Q. Wu, K. Qian, R. Bhagat, Air and PCM cooling for battery thermal management considering battery cycle life, Appl. Therm. Eng. 173 (2020), 115154.

[54] D.S. Jang, S. Yun, S.H. Hong, W. Cho, Y. Kim, Performance characteristics of a novel heat pipe-assisted liquid cooling system for the thermal management of lithium-ion batteries, Energ. Conver. Manage. 251 (2022), 115001, https://doi.org/10.1016/j.enconman.2021.115001.

[55] Y.A. Cengel, Heat Transfer Book, in, McGraw-Hill, New York, USA, 2012.

[56] J. Zhang, X. Li, G. Zhang, H. Wu, Z. Rao, J. Guo, D. Zhou, Experimental investigation of the flame retardant and form-stable composite phase change materials for a power battery thermal management system, J. Power Sources 480 (2020), 229116, https://doi.org/10.1016/j.jpowsour.2020.229116.

[57] B. Kamkari, H. Shokouhmand, Experimental investigation of phase change material melting in rectangular enclosures with horizontal partial fins, Int. J. Heat Mass Transf. 78 (2014) 839–851, https://doi.org/10.1016/j.ijheatmasstransfer.2014.07.056.

[58] C. Ji, Z. Qin, S. Dubey, F.H. Choo, F. Duan, Simulation on PCM melting enhancement with double-fin length arrangements in a rectangular enclosure induced by natural convection, Int. J. Heat Mass Transf. 127 (2018) 255–265, https://doi.org/10.1016/j.ijheatmasstransfer.2018.07.118.

[59] A. Kumar, R. Kothari, S.K. Sahu, S.I. Kundalwal, M.P. Paulraj, Numerical investigation of cross plate fin heat sink integrated with phase change material for cooling application of portable electronic devices, Int. J. Energy Res. 45 (2021) 8666–8683, https://doi.org/10.1002/er.6404.

[60] M. Barthwal, D. Rakshit, No fins attached? Numerical analysis of internal–external fins coupled PCM melting for solar applications, Appl. Therm. Eng. (2022), 118911, https://doi.org/10.1016/j.applthermaleng.2022.118911.

[61] R. da Silveira Borahel, R.D.C. Oliveski, F.S.F. Zinani, I.A. Schroer, Fin configurations to reduce lauric acid melting time in a rectangular thermal reservoir, J. Storage Mater. 44 (2021), 103339, https://doi.org/10.1016/j.est.2021.103339.